

# Planetary nebulae and stellar kinematics in the flattened elliptical galaxy NGC 1344<sup>1</sup>

A. M. Teodorescu<sup>2</sup>, R. H. Méndez<sup>2</sup>, R. P. Saglia<sup>3</sup>, A. Riffeser<sup>4</sup>, R. P. Kudritzki<sup>2</sup>, O. E. Gerhard<sup>5</sup> and J. Kley<sup>2</sup>

ana@ifh.hawaii.edu, mendez@ifh.hawaii.edu

## ABSTRACT

We present photometric and kinematic information obtained by measuring 197 planetary nebulae (PNs) discovered in the flattened Fornax elliptical galaxy NGC 1344 (also known as NGC 1340) with an on-band, off-band, grism + on-band filter technique. We build the PN luminosity function (PNLF) and use it to derive a distance modulus  $m - M = 31.4 \pm 0.18$ , slightly smaller than, but in good agreement with, the surface brightness fluctuation distance. The PNLF also provides an estimate of the specific PN formation rate:  $(6 \pm 3) \times 10^{-12}$  PNs per year per solar luminosity. Combining the positional information from the on-band image with PN positions measured on the grism + on-band image, we can measure the radial velocities of 195 PNs, some of them distant more than 3 effective radii from the center of NGC 1344. We complement this data set with stellar kinematics derived from integrated spectra along the major and minor axes, and parallel to the major axis of NGC 1344. The line-of-sight velocity dispersion profile indicates the presence of a dark matter halo around this galaxy.

*Subject headings:* galaxies: distances and redshifts — galaxies: individual (NGC1344) — galaxies: kinematics and dynamics — planetary nebulae: general — techniques: radial velocities

---

<sup>2</sup>Institute for Astronomy, University of Hawaii, 2680 Woodlawn Drive, Honolulu, HI 96822

<sup>3</sup>Max-Planck-Institut für extraterrestrische Physik, Giessenbachstraße, D-85748 Garching, Germany

<sup>4</sup>Universitäts-Sternwarte München, Scheinerstraße 1, D-81679 München, Germany

<sup>5</sup>Astronomisches Institut, Universität Basel, Venusstrasse 7, 4102 Binningen, Switzerland

<sup>1</sup>Part of the data presented herein were obtained at the European Southern Observatory, Chile, Programs ESO 67.B-0231 and 68.B-0173A.

## 1. Introduction

The currently favored hierarchical theories of galaxy formation predict that galaxies should be surrounded by dark matter halos. In particular elliptical galaxies are expected to form through merging events, and their angular momenta are expected to reside mostly in the outer halos. From the observational point of view, the existence of dark matter around some very bright elliptical galaxies is inferred from studies of hot, X-ray emitting gas (e.g., Loewenstein & White 1999) and from dynamical analyses of integrated absorption-line spectra (e.g., Gerhard et al. 2001). At the faint end, the kinematics of individual stars in the nearby Draco dwarf spheroidal offer evidence of a dark matter halo (Kleyna et al. 2002). For intermediate, “ordinary” ellipticals, the evidence is much more difficult to obtain, because they lack the hot gas and they are too distant to extract information from individual stars.

Planetary nebulae (PNs) in such elliptical galaxies offer a good alternative for dark matter studies because they are preferentially detected in the outskirts of their galaxies. A study of PNs in NGC 5128 produced some evidence of a dark matter halo (Hui et al. 1995). Everything seemed to be clear. However, more recent studies of PNs in other elliptical galaxies have raised some doubts on the ubiquity of dark matter halos in ellipticals: Méndez et al. (2001) and Romanowsky et al. (2003) could not find evidence of dark matter around 4 normal ellipticals: NGC 4697, 3379, 4494 and 821.

It is possible to argue that at least in some of these cases we may be witnessing the effect of some kind of anisotropy in the velocity distribution, for example the preponderance of radial orbits. This idea has been tested by Romanowsky et al. (2003) using an “orbit library method”, which fails again to find evidence of any cloak or shroud of dark matter around the visible mass in the case of NGC 3379. On the other hand, Milgrom & Sanders (2003) claim that the new findings confirm the predictions of Milgrom’s Modified Newtonian Dynamics (MOND) in the sense that high surface density galaxies are predicted to develop a “mass discrepancy” only at larger scaled radii.

In view of this interesting situation, we need more empirical information. This paper reports on the discovery and photometric and radial velocity measurements of PNs in the flattened Fornax elliptical galaxy NGC 1344 (also known as NGC 1340). Of intermediate mass and luminosity, this galaxy, a member of the Fornax cluster, is characterized by the presence of internal and external concentric shells (surface brightness enhancements partially encircling the galaxy) first described by Malin & Carter (1980).

We have also secured some long-slit spectrograms across NGC 1344 to improve the kinematic information close to the galaxy’s center, where the surface brightness is higher and the PNs are more difficult to find. In § 2 we describe long-slit spectrograms taken with

the Siding Spring 2.3 m telescope, and with the European Southern Observatory (ESO) Very Large Telescope (VLT), and the resulting information. Then in §§ 3 and 4 we briefly review the slitless radial velocity method, and we describe the VLT observations of PNs in NGC 1344 and the reduction procedures. Section 5 deals specifically with the PN detection and photometry. In § 6 we build the PN luminosity function and derive the PNLF distance to NGC 1344 and the specific PN formation rate. In § 7 we describe the radial velocity results, which we analyze in § 8. Section 9 gives a summary of the conclusions.

## 2. Long-slit spectrograms of NGC 1344

The major axis of NGC 1344 lies at a position angle of about 167 degrees (from north through east). Long-slit spectroscopy along the major axis of NGC 1344 was obtained in October 2001 at the Siding Spring 2.3 m telescope, using the red arm of the Double Beam Spectrograph (Rodgers et al. 1988) in longslit (6'.7) mode with 1200 R Grating ( $35.2 \text{ \AA mm}^{-1}$ ), no beamsplitter, slit width of  $4''$  and the Site  $1752 \times 532$ ,  $15\text{-}\mu\text{m}$  pixels CCD. Astigmatism along the spatial direction reduced the effective spatial resolution to  $\approx 5''$ . The wavelength range  $\lambda = 8093 - 9014 \text{ \AA}$  was covered, including the Ca Triplet region used for the kinematics. The integration time was 93 minutes. Several stars were observed, trailed along the slit, in order to use them as kinematic templates. The data reduction followed Saglia et al. (2002); see below.

Long-slit spectroscopy along the minor axis and parallel to the major axis (shifted by 16.5 arcsec to the northeast) of NGC 1344 was performed in service mode using the Focal Reducer/Spectrograph FORS2 at the Cassegrain focus of Unit Telescope 2, Kueyen, of the Very Large Telescope, Cerro Paranal, Chile, as part of Program ESO 68.B-0173A. The spectra were acquired on the 7th and 8th of January 2002 with  $0''.9$  seeing and good conditions. The grism 1400V+18 was used with a  $1''$ -wide long slit. The  $2080 \times 2048$ ,  $24 \mu\text{m}$  pixel Tektronix CCD has a  $0''.2 \text{ pix}^{-1}$  scale along the spatial direction and  $0.5 \text{ \AA pix}^{-1}$  along the dispersion direction, covering the wavelength range  $\lambda = 4770 - 5700 \text{ \AA}$  with a spectral resolution of  $2.5 \text{ \AA}$  or  $\sigma_{\text{instr}} = 63 \text{ km s}^{-1}$  (see FORS Manual, Version 2.0). The integration times were 1700 s along the major axis (P.A.= $167^\circ$ ) and 1800 s along the minor axis (P.A.= $13^\circ$ ) of NGC 1344. Template stars were also observed.

The data reduction was performed under MIDAS and followed the usual steps. After bias subtraction and flatfielding with dome flats, cosmic rays were eliminated using median filtering. The wavelength calibration was based on HeArHgCd lamps and gave  $0.5 \text{ \AA rms}$ . After rebinning on a natural logarithmic wavelength scale, the sky measured at the ends of the slit was subtracted, and the galaxy spectra were rebinned along the spatial direction to

obtain a signal-to-noise ratio nearly constant with radius. The kinematics were determined with the Fourier Correlation Quotient method, as in Bender et al. (1994) and Mehlert et al. (2000).

Statistical and systematic errors were estimated following Mehlert et al. (2000). Briefly, template stars were broadened to the observed values of  $\sigma$ ,  $h_3$ , and  $h_4$ , and noise was added to match the power spectrum noise to the peak ratio at the appropriate place. The generated spectra were analysed in the same way as the observed data, producing mean and rms values of  $V$ ,  $\sigma$ ,  $h_3$ , and  $h_4$ . The mean values reproduced the input (observed) values within the rms. These are the errors assigned to the data. For the VLT data, the statistical errors derived from Monte Carlo simulations are minute and much smaller than the rms scatter observed between the two sides of the galaxy. This can be used to set the residual systematic errors affecting the data, which amount to  $\approx 6 \text{ km s}^{-1}$  on  $V$ ,  $\approx 8 \text{ km s}^{-1}$  on  $\sigma$ , and  $\approx 0.03$  in  $h_3$  and  $h_4$ . A residual mean systematic difference between the antisymmetrized differences of the  $h_3$  values between the two sides of the galaxy of  $\approx 0.03$  points to some residual template mismatching.

Figures 1, 2, and 3 show the derived profiles. Tables 1, 2, and 3 give the data in tabular form. The parameters  $h_3$  and  $h_4$  are the amplitudes of the third- and fourth-order Gauss-Hermite functions used to describe the line-of-sight velocity distribution.

Along the minor axis, we detect a decoupled core, with the mean velocity changing sign in the inner  $2''$ . Along the major axis (or parallel to it), the  $h_3$  parameter anticorrelates with the mean velocity  $V$ , following the known local relation between  $h_3 - V/\sigma$  observed in early-type galaxies (see Bender et al. 1994). Along the minor axis,  $h_3 \approx 0$  as expected in the absence of rotation. All  $h_4$  profiles are mostly slightly negative, with the exception of the inner 7 arcsec along the minor axis, in correspondence to the decoupled core. Such negative  $h_4$  profiles are not observed very often in early-type galaxies, and suggest an interesting orbital structure to be investigated with proper modeling in the future (see, for example, Thomas et al. 2005).

### 3. On PN detection and slitless radial velocities

For the detection of PNs belonging to NGC 1344, we used the classical on-band, off-band method. The method is based on blinking two images: an on-band image taken through a narrow-band filter passing the redshifted [O III]  $\lambda 5007$  nebular emission line, and an off-band image taken through a broader filter passing no strong nebular emissions. The PNs, which are point sources, are visible in the on-band image but must be absent in the off-band image,

which should be exposed a bit deeper for unambiguous detections.

Taking a third image through the on-band filter and a grism helps with the identification of the PN candidates. As a consequence of inserting the grism into the light path, the images of all continuum sources are transformed into segments of width determined by the on-band filter transmission curve, while the PNs and any other emission-line point sources remain point sources. But in addition, and most important, the grism introduces a shift relative to the undispersed on-band image. The shift is a function of the wavelength of the nebular emission line and of position on the CCD. Once we measure and calibrate the shift, we can calculate the emission-line wavelength for all detected sources, and finally we obtain their radial velocities irrespective of the number of sources and their distribution in the field. This method has already been used to discover and measure the radial velocities of 535 PNs in the elliptical galaxy NGC 4697 (Méndez et al. 2001; hereafter Paper I). Please refer to Paper I for a detailed description of the calibration procedures.

#### 4. PN search: VLT observations and reductions

Since the major axis of NGC 1344 is close to the north-south direction, we decided to expose two partly overlapping fields, north and south, both containing the center of the galaxy. For simplicity, we call the two fields N and S.

The observations were made with the first Focal Reducer/Spectrograph (FORS1) at the Cassegrain focus of Unit Telescope 3, Melipal, of the ESO Very Large Telescope, Cerro Paranal, Chile, on three second-half-nights, 2001 September 22/23/24. FORS1, with the standard collimator, gives a field of  $6'.8 \times 6'.8$  on a  $2080 \times 2048$  CCD (pixel size  $24 \times 24 \mu\text{m}$ ). The image scale is  $0''.2 \text{ pix}^{-1}$ . Direct imaging was done through interference filters. The on-band and off-band filters used for NGC 1344 have the following characteristics: effective central wavelength in observing conditions of 5030 and 5300 Å, peak transmissions of 0.83 and 0.85, equivalent widths of 48.5 and 215 Å, and FWHMs of 60 and 250 Å. The dispersed images were obtained with grism 600B. This grism gives a dispersion of  $50 \text{ Å mm}^{-1}$ , or  $1.2 \text{ Å pix}^{-1}$ , at 5000 Å.

Table 4 shows the CCD images used for data reduction analysis. They can be grouped as follows:

1. Off-band, on-band, and (grism + on-band) images of the NGC 1344 N field.
2. Off-band, on-band, and (grism + on-band) images of the NGC 1344 S field.
3. On-band and (grism + on-band) multislit images and comparison lamp spectra

through 10 different vertical arrangements of the 19 FORS slitlets for the wavelength calibration.

4. On-band and (grism + on-band) multislit images and spectra of the Galactic PN NGC 7293 (PN G036.1-57.1) in six different positions across the CCD for complementary calibration purposes described in Paper I. These observations were done through another on-band filter with an effective central wavelength of 4992 Å and FWHM=60 Å.

5. On-band (5030 Å) images of the spectrophotometric standard LTT 9491 (Oke 1990) for the photometric calibration.

The three allocated half-nights were dark and of photometric quality, with seeing around 0".6, 1".1, and 0".8 on the first, second, and last night, respectively.

The basic CCD reductions (bias subtraction, flat-field correction using twilight flats) were made using IRAF<sup>6</sup> standard tasks. Image combinations, required to eliminate cosmic ray events and enable detection of faint PNs, were made in the following way: First, for each field, N and S, one pair of (undispersed, dispersed) on-band individual images of the best possible quality, and taken consecutively at the telescope, was adopted as reference images. For the S field, the reference images were 22T06:41 (on-band) and 22T07:08 (grism+on-band) (see Table 4). For the N field, the reference images were 24T08:00 (on-band) and 24T08:27 (grism+on-band). All the other available images, including the off-band ones, were registered upon the corresponding reference image. In this way, any possible displacements produced by guiding problems or deformations in the spectrograph were reduced to a minimum. The registration was done with IRAF tasks “geomap” and “gregister”. The registration of the undispersed S field was very good; using 113 stars, the residuals were not larger than 0.1 pixel. For the registration of the undispersed N field, 114 stars were used, but the residuals were up to 0.2 pixel because some of the N images were more affected by poor seeing.

Registration of the dispersed images was more difficult. From previous experience in Paper I we know that it is better to register using the brightest PN images, avoiding any temperature-dependent shifts in the positions of the spectral segments produced by normal stars. For that reason, we registered the N field using the 28 brightest PNs (visible in the individual grism+on-band images). For the S field, the corresponding number was 25 PNs. The resulting residuals in both cases were smaller than 0.3 pixel. Since an error of 0.3 pixel in the distance between undispersed and dispersed images would produce an error of 20 km

---

<sup>6</sup>IRAF is distributed by the National Optical Astronomical Observatories, which are operated by the Association of Universities for Research in Astronomy, Inc., under cooperative agreement with the National Science Foundation.

$\text{s}^{-1}$  in radial velocity for the grism dispersion of  $50 \text{ \AA mm}^{-1}$ , we can estimate that a typical internal error in an individual measurement is not larger than  $20 \text{ km s}^{-1}$ . Having obtained a satisfactory registration, we produced the combined on-band, off-band and dispersed images for the N and S fields using the IRAF task “imcombine”.

For easier PN detection and photometry in the central parts of NGC 1344, where the background varies strongly across the field, we produced images showing the differences between undispersed on-band and off-band combined frames. In ideal conditions, this image subtraction should produce a flat noise frame with the emission-line sources as the only visible features. A critical requirement to achieve the desired result is perfect matching of the PSFs of the two frames to be subtracted. For this purpose, we applied a method for “optimal image subtraction” developed by Alard & Lupton (1998) and implemented in Munich by Gössl & Riffeser (2002) as part of their image reduction pipeline. Figures 4 and 5 show sections of the resulting difference images in the N and S fields.

This procedure cannot be used for the combined dispersed images because there is no off-band counterpart. Therefore, to flatten the background and reduce the contamination of the fields by the stellar spectra, we applied the IRAF task “fmedian” to the combined N and S dispersed images, with a box of  $17 \times 17$  pixels. The resulting medianed images were subtracted from the unmedianed ones. Figures 6 and 7 show the result for the corresponding fields shown in Figures 4 and 5.

## 5. PN detection and photometry

The PN detection requires the identification of the candidates in both the undispersed and dispersed images. In addition, the object has to be a point source and must be undetectable in the off-band image. This is required to minimize the confusion with emission-line sources in background galaxies. The PN candidates were found by blinking the on-band versus the off-band difference images and confirmed by blinking on-band versus dispersed. The  $(x, y)$  pixel coordinates of all the candidates in the undispersed and dispersed images were measured with the IRAF task “phot” with the centering algorithm “centroid”. We found a total of 197 PN candidates, which are listed in Table 5. In §7 we will describe the procedure for radial velocity determinations; here we present the on-band photometry.

We express the  $\lambda 5007$  fluxes in magnitudes  $m(5007)$  using the definition introduced by Jacoby (1989),

$$m(5007) = -2.5 \log I(5007) - 13.74 \quad (1)$$

For the flux calibration, we adopted the standard star LTT 9491 (Oke 1990). This star has a monochromatic flux at 5030 Å of  $1.033 \times 10^{-14}$  ergs cm<sup>-2</sup> s<sup>-1</sup> Å<sup>-1</sup>. The flux measured through the on-band filter in units of ergs cm<sup>-2</sup> s<sup>-1</sup> can be calculated knowing the equivalent width of the on-band filter; using equation (1), we find  $m(5007)=17.01$  for LTT 9491.

Since most PNs were measurable only on the differences of combined images (on–off), to calculate the  $m(5007)$  of the PNs we had to proceed through several steps. First, we made aperture photometry of LTT 9491 using the IRAF task “phot”. The FWHM of LTT 9491 was between 3 and 4.5 pixels. We adopted an aperture radius of 16 pixels; the sky annulus had an inner radius of 21 pixels and a width of 5 pixels. The same parameters were used to make aperture photometry of several moderately bright stars in the reference images corresponding to both fields (24T08:00 for the north field and 22T06:41 for the south field). Seven and six stars were selected in the N and S fields, respectively. Three of these stars were common to both fields. These three “internal standards” are between 2 and 3 mag fainter than LTT 9491, and they are distant from the center of NGC 1344, so that background problems are avoided.

Having tied the spectrophotometric standard to the internal frame standards, we switched to strictly differential photometry. We made aperture photometry of the “internal standards” on the N and S on-band combined images; the sky annulus had an inner radius of 11 pixels and a width of 9 pixels. On the same on-band combined images, we subsequently made PSF-fitting daophot photometry (Stetson 1987; IRAF tasks “phot”, “psf” and “allstar”) of the “internal standards” and four bright PNs. From the aperture photometry and PSF-fitting photometry of the “internal standards”, we determined the aperture correction. As a last step, we made PSF-fitting photometry of all PN candidates on the difference images (on-band minus off-band), where, of course, no stars remain. The four bright PNs were used to tie this photometry to that of the standards. We estimate internal errors in the photometry of the difference images below 3%.

To obtain physical fluxes, we needed the on-band filter peak transmission (see, e.g., Jacoby et al. 1987). For this purpose we used the method described in Paper I. No correction to the photometry as a function of redshift was necessary; given the observed velocities, to be reported later, none of our objects is shifted away from the flat peak of the on-band filter transmission curve. A good way of testing the reliability of the photometry is to plot the S on-band magnitudes  $m(5007)$  as a function of the N on-band magnitudes for the 132 objects measured in both fields. From the dispersion in Figure 8, we estimate rms errors of 0.16 and 0.24 mag for  $m(5007)$  brighter and fainter than 27.5, respectively. For each of these 132 PNs, we have adopted the average of the two  $m(5007)$  measurements.



## 6. The PNLF, distance, and PN formation rate

Once the apparent magnitudes  $m(5007)$  were measured, the PN luminosity function (PNLF) was built. We followed the same procedure described in Paper I. Only those PNs brighter than  $m(5007) = 28$  were used to build the PNLF. The zone of exclusion at the center of NGC 1344, which we introduce to eliminate regions of very high surface brightness, where PN detection is more difficult, is an ellipse with (minor, major) semiaxes of (250, 350) pixels (the image scale is  $0''.2 \text{ pix}^{-1}$ ). After eliminating the PNs within the exclusion ellipse and those that are too faint, we were left with 91 PNs. The statistically complete PNLF is plotted in Figure 9. The absolute magnitudes  $M(5007)$  were derived using an extinction correction of 0.066 mag (from data listed in NED, the NASA/IPAC Extragalactic Database; see Schlegel et al. 1998) and adopting a distance modulus  $m - M = 31.38$ , which produces the best fit. The observed PNLF was fitted with simulated PNLFs like the one used by Méndez & Soffner (1997) to fit the observed PNLF of M 31. The simulated PNLFs plotted in Figure 9 are binned, like the observed one, into 0.2 mag intervals and have a maximum final mass of  $0.63 M_{\odot}$ ,  $\mu_{\text{max}} = 1$ , and sample sizes between 1500 and 4000 PNs (see Méndez & Soffner 1997; the “sample size” is defined as the total number of PNs, detected or not, that exist in the surveyed area). The observed PNLF in Figure 9 presents an evident change of slope, thus making possible an unambiguous determination of distance and sample size. From the goodness of the fit at different distance moduli, we derived an internal error of 0.1 mag in distance modulus. For the total error estimate, we have to add possible systematic and random errors. The possible systematic error is the same as in Jacoby et al. (1990), i.e., 0.13 mag, including the possible error in the distance to M 31, in the modeling of the PNLF and in the foreground extinction. The random contributions in our case are 0.1 mag from the fit to the PNLF, as mentioned above, 0.05 mag from the photometric zero point, and 0.05 mag from the filter calibration. Combining all these errors quadratically, we estimate that the total error bar for the distance modulus must be  $\pm 0.18$  mag. Our distance modulus 31.38 is equivalent to 18.9 Mpc. Our PNLF distance modulus for NGC 1344 is a bit larger than, but in reasonable agreement with, the PNLF distance moduli of the Fornax galaxies NGC 1316, 1399 and 1404 (31.13, 31.17, and 31.15, respectively; see McMillan et al. 1993).

We find good agreement, within the uncertainties, with the SBF distance modulus  $31.48 \pm 0.3$  reported by Tonry et al. (2001) for NGC 1344. Note, however, that the PNLF distance is slightly shorter than the SBF distance. This small, still unexplained, discrepancy happens in many other cases; see Méndez (1999) and Ciardullo et al. (2002).

Knowing the sample size, we can estimate the specific PN formation rate  $\dot{\xi}$  in units of PNs  $\text{yr}^{-1} L_{\odot}^{-1}$

$$n_{\text{PN}} = \dot{\xi} L_{\text{T}} t_{\text{PN}} \quad (2)$$

where  $n_{\text{PN}}$  is the sample size,  $L_{\text{T}}$  is the total bolometric luminosity of the sampled population expressed in  $L_{\odot}$ , and  $t_{\text{PN}}$  is the lifetime of a PN, for which we have adopted 30,000 yr in the PNLF simulations. We have  $B_{\text{T}} = 11.27$ ,  $B - V = 0.87$  (de Vaucouleurs et al. 1991),  $A_{\text{B}} = 0.08$  (again from the NASA/IPAC Extragalactic Database), and a bolometric correction of  $-0.78$  mag from which we obtain an extinction-corrected apparent bolometric magnitude 9.54. Using a distance modulus of 31.38 and a solar  $M_{\text{bol}} = 4.72$ , we calculate the total luminosity of NGC 1344,  $4.2 \times 10^{10} L_{\odot}$ . The central ellipse, which we excluded, contributes 70% of the total luminosity, so the sampled luminosity is  $L_{\text{T}} = 1.3 \times 10^{10} L_{\odot}$ . Adopting  $n_{\text{PN}} = 2300$  from Figure 9, we obtain  $\dot{\xi} = (6 \pm 3) \times 10^{-12}$ . This is the same PN formation rate obtained for NGC 4697 in Paper I.

## 7. Radial velocities: results and discussion

From now on, we will refer to heliocentric radial velocities determined with the slitless method simply as “velocities”. We consider first the information provided by the calibration exposures of NGC 7293. This local PN has such a large angular size that it allows us to obtain calibration measurements all across the CCD in a few exposures (see Paper I). Figure 10 shows the velocities in NGC 7293 measured at 114 positions across the CCD, using a similar distribution as used in Paper I. The behavior of these velocities is very similar to what is shown in Figure 16 of Paper I. We therefore adopted the same empirical correction described in Paper I, which was designed to give the expected NGC 7293 radial velocity ( $-20 \text{ km s}^{-1}$ ) irrespective of the position on the CCD. The result of applying the correction is shown in Figure 11. Our calibration gives velocities with errors below  $20 \text{ km s}^{-1}$ .

For NGC 1344, if we add quadratically the calibration errors and the errors from image registration (§3), we get errors of about  $30 \text{ km s}^{-1}$ . There is still another source of errors: spectrograph deformations and guiding problems during long exposures. The only way of testing the impact of these kind of errors is to compare velocities obtained from different pairs of (undispersed, dispersed) long exposures. For this purpose, the redundancy between the N and S fields becomes useful. In Figure 12 we compare the velocities of 128 PNs measured in both fields. The standard deviation is  $34 \text{ km s}^{-1}$ . Therefore spectrograph deformations and guiding errors have at most a marginal contribution to the total uncertainty in the velocities, which we conservatively estimate to be  $40 \text{ km s}^{-1}$ . For the velocities of the 128 PNs measured twice, we adopted the average of N and S measurements.

We could measure the velocities of 195 of the 197 PN candidates in NGC 1344. Their velocities are in the range from 900 to 1500 km s<sup>-1</sup>. In addition to the 197 PN candidates, we also found one object with a velocity of 770 km s<sup>-1</sup>, which is too small. We have rejected it as a PN; it is most probably a background emission-line galaxy with a redshifted emission line shining through the on-band filter. We cannot exclude the existence of a few other background emission-line sources with the “right” velocity contaminating our PN sample, but the surface density of these background sources is too small to have any effect on our conclusions regarding the PN kinematics.

Figure 14 shows the (x, y) coordinates of the 195 PNs with respect to the center of light of NGC 1344. The position of this center can be measured with errors below 1 pixel. We have defined the x-axis along the major axis of NGC 1344. Figure 13 shows the velocities of the 195 PNs as a function of the x coordinate in arcsec, and Figure 15 shows the same 195 velocities as a function of the y coordinate. The average velocity of the 195 PNs is 1188 km s<sup>-1</sup>, in good agreement with the NED radial velocity of 1169 km s<sup>-1</sup>. Our NGC 1344 velocity from the PNs has an uncertainty of 15 km s<sup>-1</sup> if we take into account a velocity dispersion of the order of 150 km s<sup>-1</sup> (see next section), the number of PNs measured, and the possible systematic error of  $\pm 10$  km s<sup>-1</sup> in our velocities from the calibration procedure using NGC 7293.

## 8. Rotation and line-of-sight velocity dispersion

We investigated rotation by dividing the 195 PNs into six subsamples along the x-axis and calculating the average velocity for each subsample. Because the signature of rotation can be diluted if the subsamples extend too much in the y direction, we restricted our selection to a small range of y values, that is, to within 20'' from the major axis. Figure 16 compares the resulting run of average PN velocity along the major axis with the information derived earlier from the long-slit spectra (Figures 3 and 1). The integrated absorption-line spectra indicate some rotation along the major axis (south receding), and indeed the rotation on the major axis appears to be a bit faster than away from the major axis. But the restriction to PNs close to the major axis produces numbers too small in each subsample, and therefore, large error bars. The PNs appear to be indicating the same sense of rotation as the integrated spectra, but with marginally lower amplitude. However, the error bars are too large to say much about rotation along the major axis beyond two effective radii from the PN velocities. In Figure 2 we also see some rotation along the minor axis (east approaching). The PNs cannot confirm this weak rotational signal (see Figure 15); the line-of-sight velocity dispersion is too large near the center.

To study the run of the line-of-sight velocity dispersion as a function of angular distance from the center, we divided the 195 PNs into five subsamples: one at the center of the galaxy and the other four in two pairs, north and south, progressively more distant from the center, to minimize the effect of rotation on the dispersions. The numbers of PNs within each zone are listed in the caption to Figure 17, where we show the resulting line-of-sight velocity dispersions, which have been corrected to compensate for the effect of measurement errors of  $40 \text{ km s}^{-1}$ . We also show the velocity dispersions derived earlier from the long-slit spectra (Figures 1-3, and Tables 1-3). We have plotted both the major and minor axis absorption-line dispersion data in Figure 17, because their average is closer to the averaging in circular shells done for the PNs. We find marginal agreement, within error bars, between PN and absorption-line data within  $50''$  of the galaxy’s center. Outside, the last few dispersions from absorption-line data are very high, but considering the spread in dispersions from absorption-line data at different positions, we again find marginal agreement with the PN data.

We first tried to fit the run of line-of-sight velocity dispersion with distance from the center of NGC 1344 using an analytical model proposed by Hernquist (1990). This model is spherical, nonrotating, and isotropic, and it assumes a constant mass-to-light ratio. It worked very well in the case of NGC 4697 (Paper I). Figure 17 shows that this model fails for NGC 1344. The fit at the center was obtained by adopting a total mass of  $1.5 \times 10^{11} M_{\odot}$  and an effective radius  $R_e = 46''$ , which is equivalent to 4.2 kpc for the distance modulus  $m - M = 31.38$ . The observed dispersion lies consistently above the Hernquist model beyond  $3 R_e$ , giving evidence of a dark matter halo around NGC 1344. To model this dark matter halo, we adopted a two-component Hernquist mass distribution (Hui et al. 1995, Eq. 8):

$$M(r) = \frac{M_l r^2}{(r + a)^2} + \frac{M_d r^2}{(r + d)^2} \quad (3)$$

where  $M_l$  and  $M_d$  are the visible and dark matter total masses, and  $a$  and  $d$  are the corresponding scale lengths. Given the corresponding density and potential, we computed the projected velocity dispersion as a function of distance from the center using a code that numerically integrates the Jeans equation and expands the resulting three-dimensional and projected dispersions in Chebyshev polynomials. The two-component Hernquist model successfully fits the observed line-of-sight velocity dispersion, as shown in Figure 17, if we adopt the following parameters:  $M_l = (1.4 \pm 0.2) \times 10^{11} M_{\odot}$ ,  $M_d = (3.8 \pm 0.8) \times 10^{11} M_{\odot}$ , and  $d = (17 \pm 5) a$  (note that in the Hernquist model,  $R_e = 1.8153 a$ ). We do not attribute a lot of significance to the numerical values of these parameters; we are content with the implication that there seems to be a dark matter halo in the outskirts of NGC 1344, in interesting contrast to the evidence in other galaxies like NGC 4697.

There is a caveat in that we are using a spherically symmetric model to study a galaxy that is obviously flattened. So let us briefly discuss what is the effect of using a spherical Hernquist model for this flattened galaxy. NGC 1344 is E5, probably quite edge-on, probably triaxial from the minor axis rotation in Figure 2. The major and minor axes of the triaxial distribution are likely to be nearly in the plane of the sky. In this case, edge-on oblate models fitting the projected major axis line-of-sight motions will slightly underestimate the kinetic energy in the equatorial plane, thus giving a useful lower limit to the enclosed mass. Figure 8 of Dehnen & Gerhard (1994) shows that spherical and flattened isotropic oblate models of the same cuspy mass distribution have very similar shapes in their velocity dispersion profiles on the major and minor axes. For these isotropic rotators, most of the extra gravity in the flattened distribution of the same mass goes into rotation. In addition, the gravitational potential of a flattened Hernquist profile at  $3R_e$  is only mildly non-spherical. This suggests that fitting a spherical model to the velocity dispersion profile shape is a reasonable approximation, and that the discrepancy of the PN velocities at  $3R_e$  from this profile is significant.

We also need to discuss the possibility of some degree of tangential anisotropy in the stellar orbital distribution; an excess of tangential motions could work in the same sense as a dark matter halo to produce an excess of line-of-sight velocity dispersion in the galaxy outskirts. However, in Figure 18, a graph of the number of PNs as a function of velocity does not show the flat-topped distribution we could expect from a substantial excess of tangential orbits at large angular distances from the center (see, e.g., Figure 10 in Dehnen & Gerhard 1993). This suggests that anisotropy effects, if present, do not affect our qualitative conclusion about dark matter around this galaxy.

Using our estimate of the visible mass, we can estimate the  $M/L$  ratio in blue light. Knowing the extinction-corrected  $B_T=11.14$ , the distance modulus 31.4, and the solar  $B$  absolute magnitude 5.48, we obtain for NGC 1344 a blue luminosity of  $2 \times 10^{10}$  solar luminosities, which gives  $(M/L)_B=7$ .

As we collect more information, some degree of variety in the amount and/or distribution of dark matter appears to be emerging. Gerhard et al. (2001) have reported a spread in the luminous-to-dark matter ratio in giant ellipticals, showing that some galaxies have no indication of dark matter within  $2 R_e$ , while others do have. We seem to be finding a similar situation in less luminous ellipticals like NGC 4697 and NGC 1344. Better modeling of the data set that takes into account the flattening of the galaxy and the stellar orbital distribution will be needed to more properly assess this conclusion. In a future paper, we expect to apply triaxial models, currently in preparation, to this problem.

We will need data for many other elliptical galaxies before a clearer picture can be

formed. Fortunately, the PN families in the outskirts of elliptical galaxies look very promising as a source of important and unique kinematic information.

## 9. Summary of conclusions

We have detected 197 PNs in NGC 1344, and have measured their brightnesses and radial velocities. We also measured stellar kinematics from long-slit integrated spectra along the major and minor axes, and parallel to the major axis of NGC 1344.

The [O III]  $\lambda 5007$  PNLF permits us to estimate a distance modulus  $m - M = 31.4 \pm 0.2$ , in good agreement with, but slightly smaller than the surface brightness fluctuation distance of Tonry et al. (2001). We also obtain a rather typical PN formation rate of  $6 \times 10^{-12}$  PNs  $\text{yr}^{-1} L_{\odot}^{-1}$ . The slitless PN radial velocities do not permit us to set any strong constraint on the rotation of NGC 1344, but the behavior of the line-of-sight velocity dispersion as a function of distance from the center of the galaxy gives evidence of the existence of a dark matter halo around this galaxy.

This work was supported by the National Science Foundation (USA) under Grant No. 0307489. We thank M. Colless, who performed the Siding Spring long-slit observations presented in § 2. RPS and AR acknowledge support by the DFG grant SBF 375, and OEG by grant 200020-101766 from the Swiss National Science Foundation. We thank the anonymous referee for some useful suggestions.

## REFERENCES

- Alard, C., & Lupton, R.H. 1998, ApJ, 503, 325
- Bender, R., Saglia, R.P., & Gerhard, O.E. 1994, MNRAS, 269, 785
- Ciardullo, R., Feldmeier, J.J., Jacoby, G.H. et al. 2002, ApJ, 577, 31
- Dehnen, W., & Gerhard, O.E. 1993, MNRAS, 261, 311
- Dehnen, W., & Gerhard, O.E. 1994, MNRAS, 268, 1019
- de Vaucouleurs, G. et al. 1991, Third Reference Catalogue of Bright Galaxies (New York: Springer)
- Gerhard, O., Kronawitter, A., Saglia, R., & Bender, R. 2001, AJ, 121, 1936

- Gössl, C.A., & Riffeser, A. 2002, *A&A*, 381, 1095
- Hernquist, L. 1990, *ApJ*, 356, 359
- Hui, X., Ford, H.C., Freeman, K.C., & Dopita, M.A. 1995, *ApJ.*, 449, 592
- Jacoby, G.H. 1989, *ApJ*, 339, 39
- Jacoby, G.H., Ciardullo, R., & Ford, H.C. 1990, *ApJ*, 356, 332
- Jacoby, G.H., Quigley, R.J., & Africano, J.L. 1987, *PASP*, 99, 672
- Kleyna, J., Wilkinson, M.I., Evans, N.W., Gilmore, G., & Frayn, C. 2002, *MNRAS*, 330, 792
- Loewenstein, M., & White, R. E. 1999, *ApJ*, 518, 50
- Malin, D.F., & Carter, D. 1980, *Nature*, 285, 643
- McMillan, R., Ciardullo, R., & Jacoby, G.H. 1993, *ApJ*, 416, 62
- Mehlert, D., Saglia, R.P., Bender, R., & Wegner, G. 2000, *A&AS*, 141, 449
- Méndez, R.H. 1999, in *Post-Hipparcos Cosmic Candles*, ed. A. Heck & F. Caputo (Dordrecht: Kluwer), 161
- Méndez, R.H., Riffeser, A., Kudritzki, R.P., et al. 2001, *ApJ*, 563, 135
- Méndez, R.H., & Soffner, T. 1997, *A&A*, 321, 898
- Milgrom, M., & Sanders, R.H. 2003, *ApJ*, 599, L25
- Oke, J.B. 1990, *AJ*, 99, 1621
- Rodgers, A.W., Conroy, P., & Bloxham, G. 1988, *PASP*, 100, 626
- Romanowsky, A.J., Douglas, N.G., Arnaboldi, M., et al. 2003, *Science*, 301, 1696
- Saglia, R.P., Maraston, C., Thomas, D., Bender, R., & Colless, M. 2002, *ApJ*, 579, L13
- Schlegel, D.J., Finkbeiner, D.P., & Davis, M. 1998, *ApJ*, 500, 525
- Stetson, P.B. 1987, *PASP*, 99, 191
- Thomas, J., Saglia, R.P., Bender, R. et al. 2005, *MNRAS*, 360, 1355
- Tonry, J.L., Dressler, A., Blakeslee, J.P. et al. 2001, *ApJ*, 546, 681

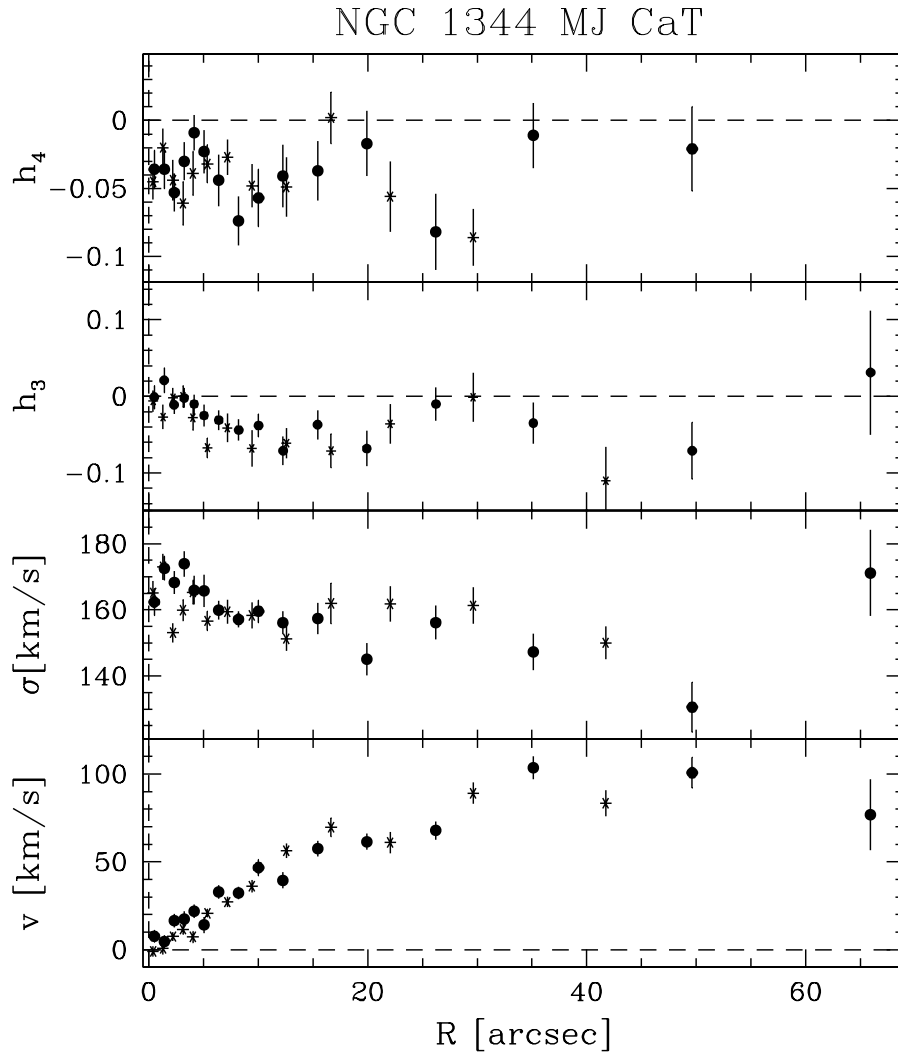


Fig. 1.— Folded kinematics along the major axis of NGC 1344 (CaT data). Filled symbols are to the south and receding.



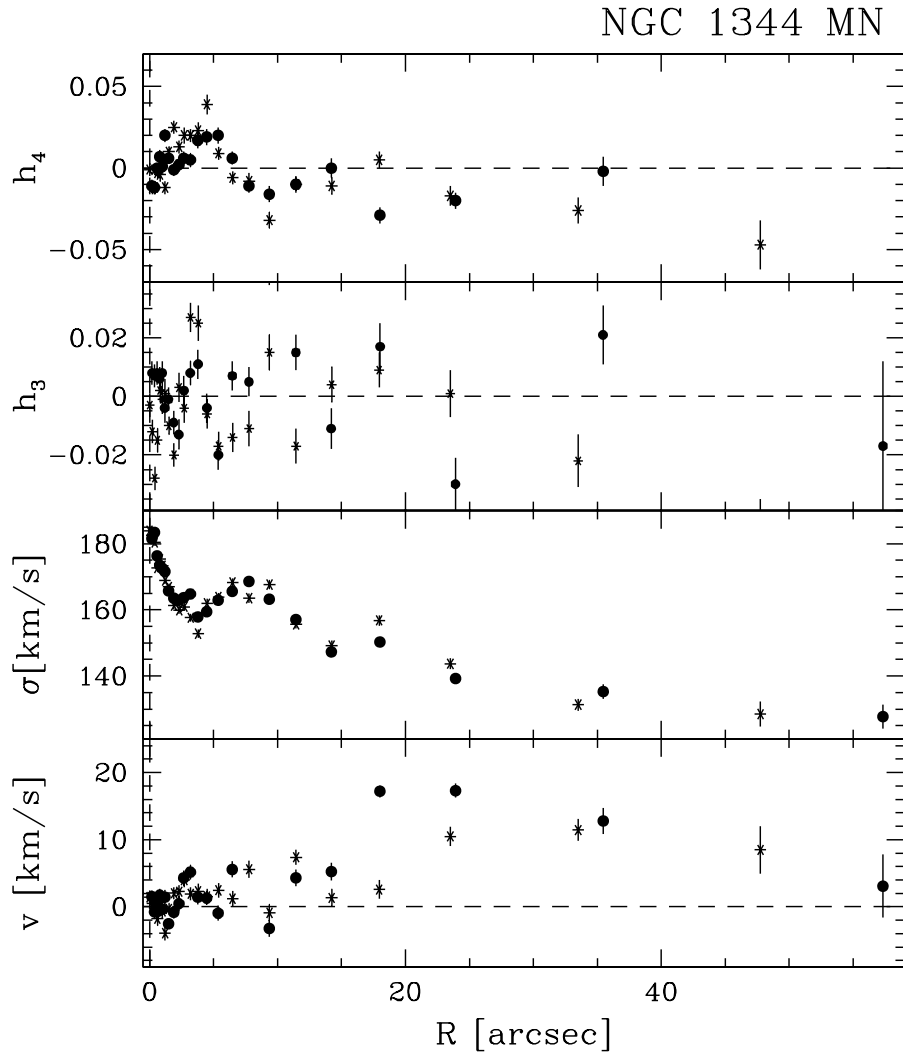


Fig. 2.— Folded kinematics along the minor axis of NGC 1344 (FORS data). Filled symbols are to the east and approaching.

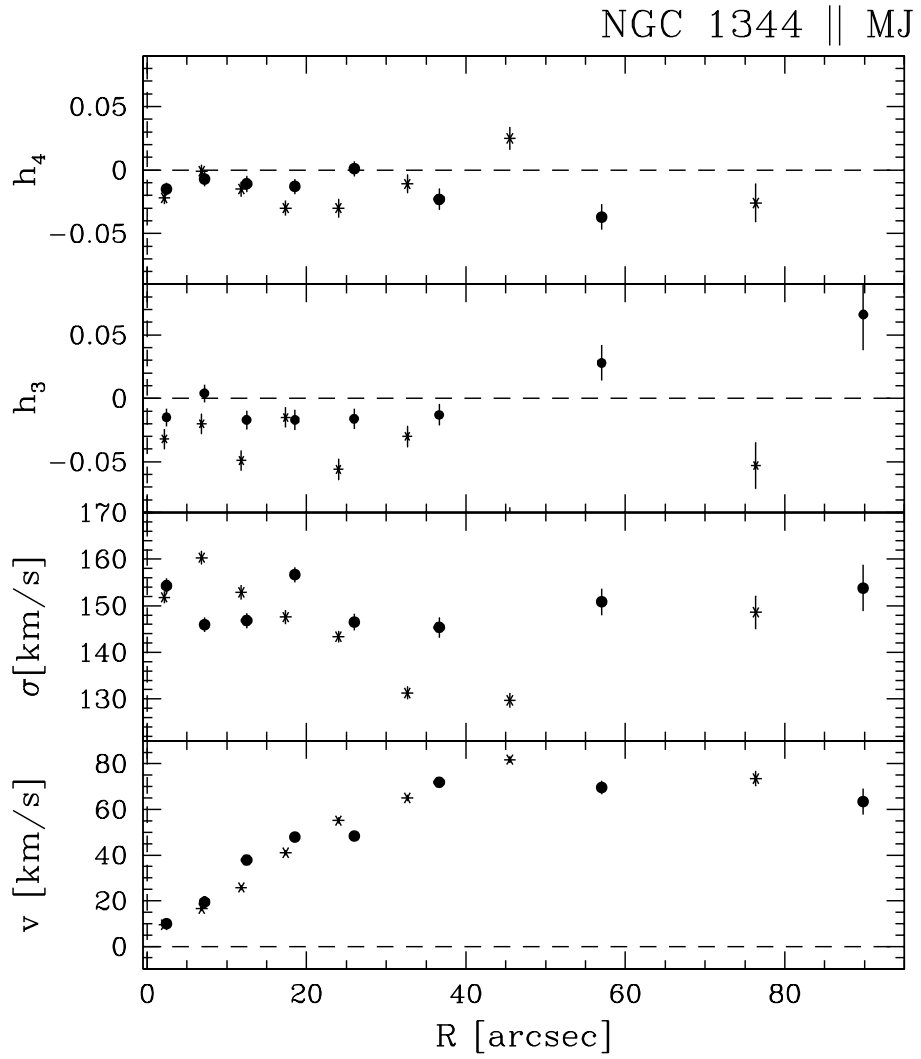


Fig. 3.— Folded kinematics parallel to the major axis of NGC 1344 (FORS data). Filled symbols are to the south and receding.

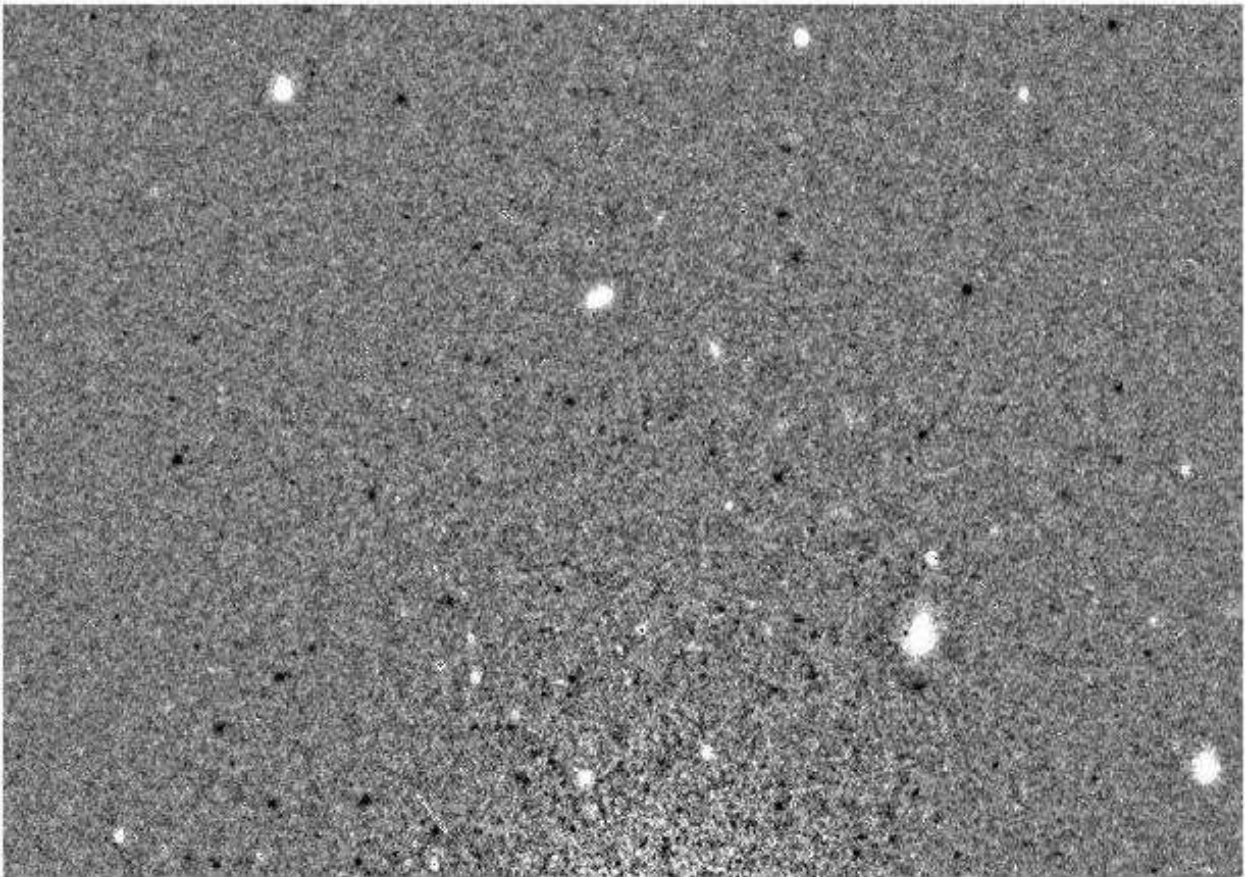


Fig. 4.— NGC 1344, difference image (on – off), part of the north field. The center of the galaxy lies just below the bottom of this image. The PNs appear as black dots.

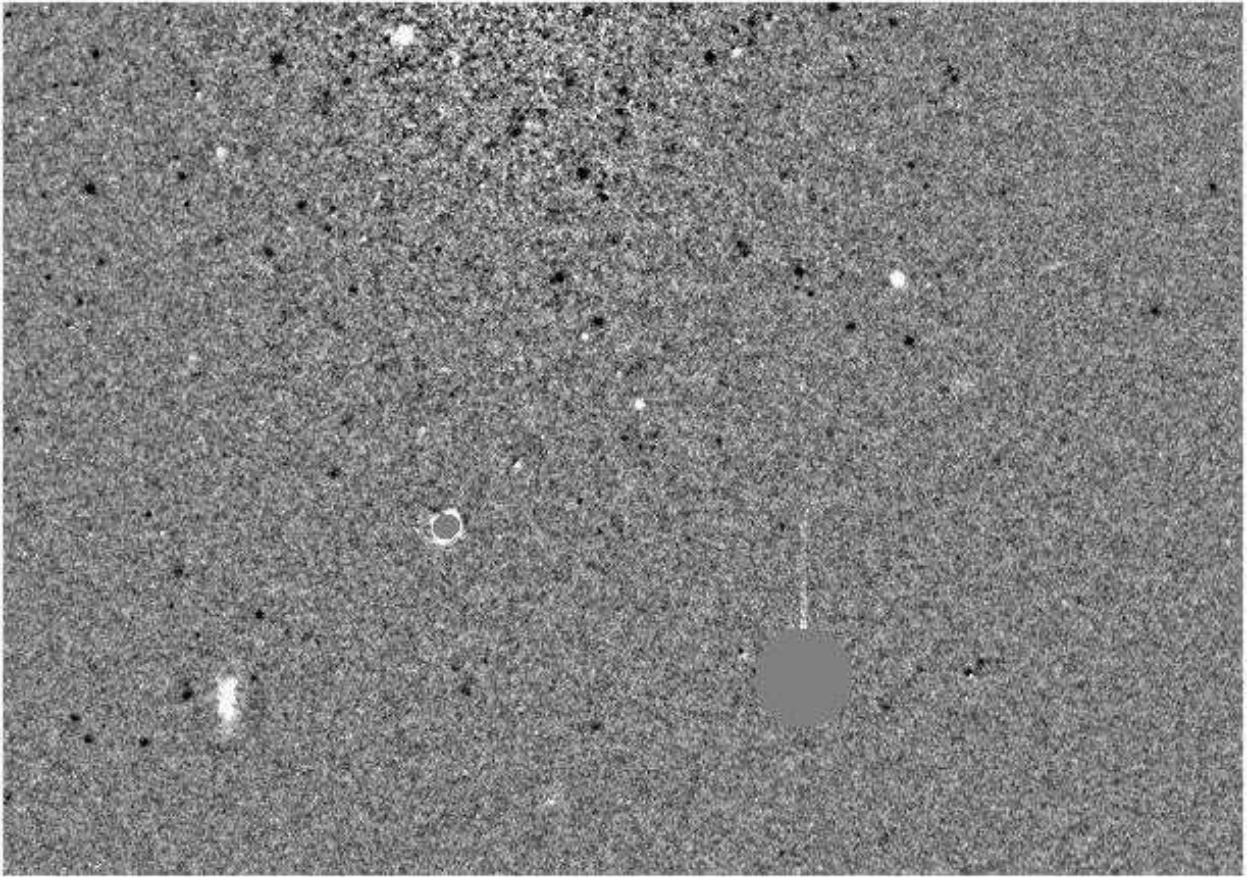


Fig. 5.— NGC 1344, difference image (on – off), part of the south field. The center of the galaxy lies just above the top of this image. The PNs appear as black dots.

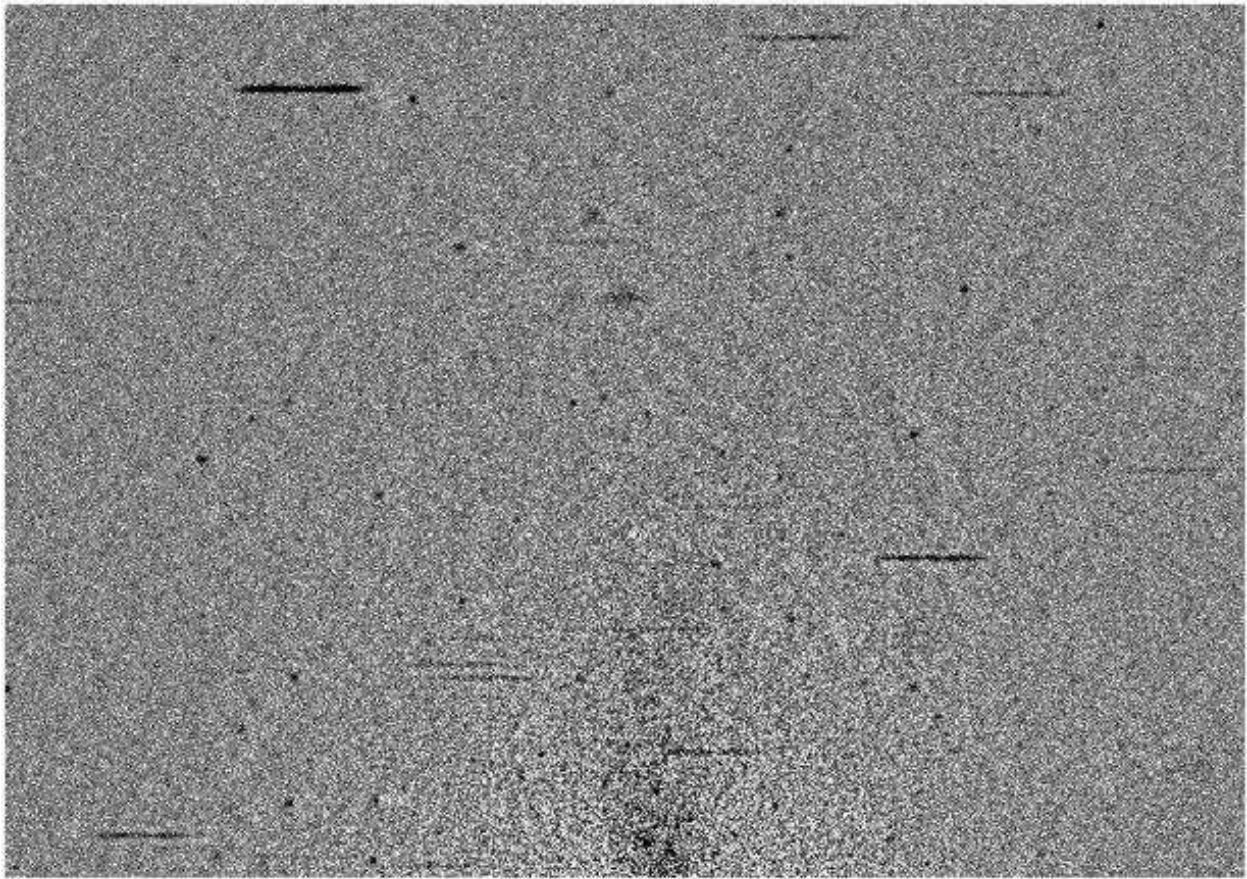


Fig. 6.— NGC 1344, difference grism image (unmedianed - medianed). This is the same part of the north field shown in Fig. 4

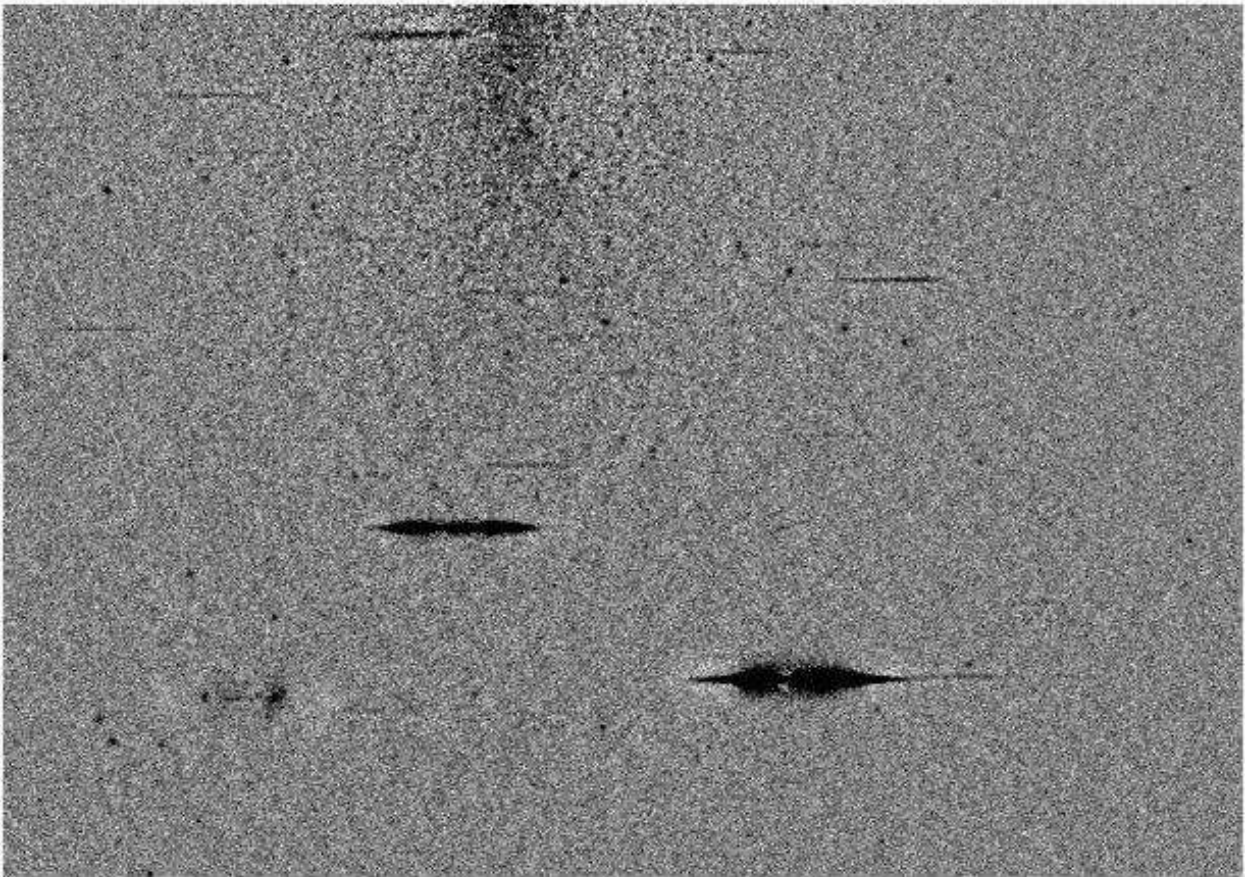


Fig. 7.— NGC 1344, difference grism image (unmedianed – medianed). This is the same part of the south field shown in Fig. 5

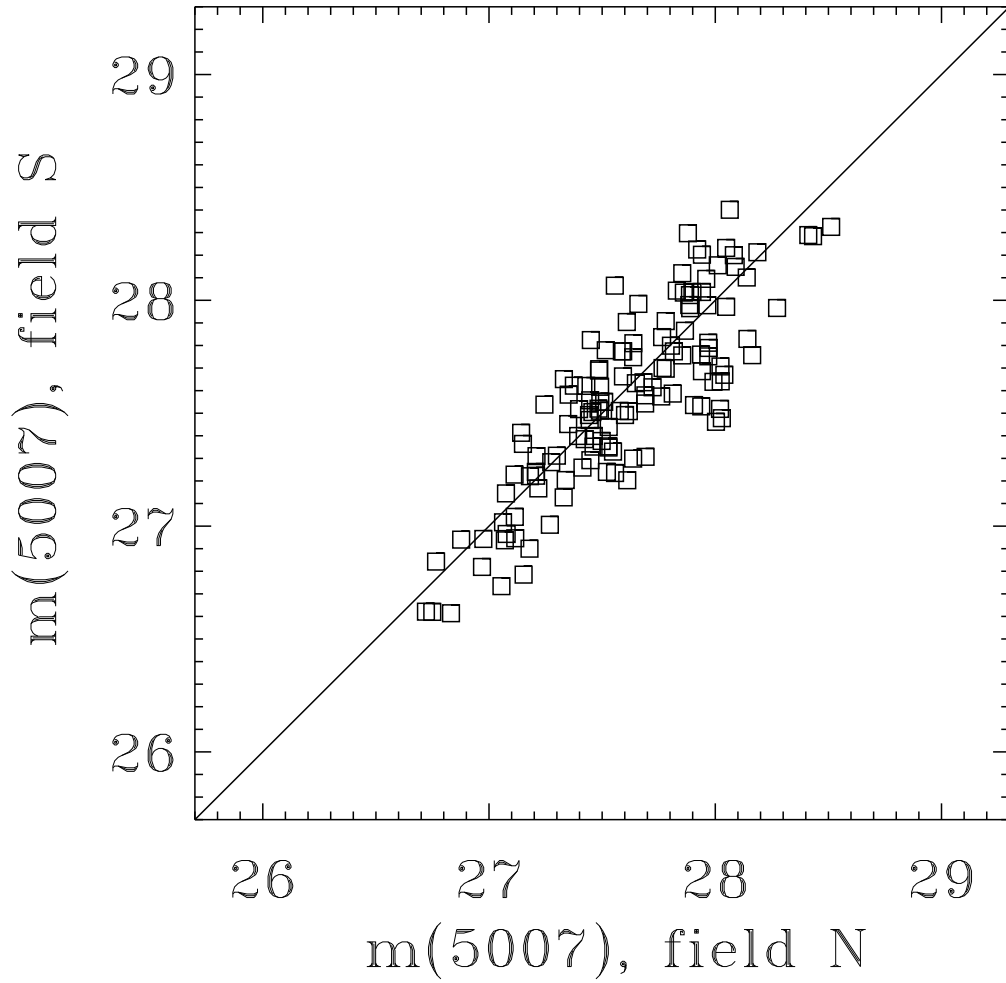


Fig. 8.— Magnitudes  $m(5007)$  of 132 PNs measured in both fields N and S. We estimate rms errors of 0.16 and 0.24 mag for  $m(5007)$  brighter and fainter than 27.5, respectively.

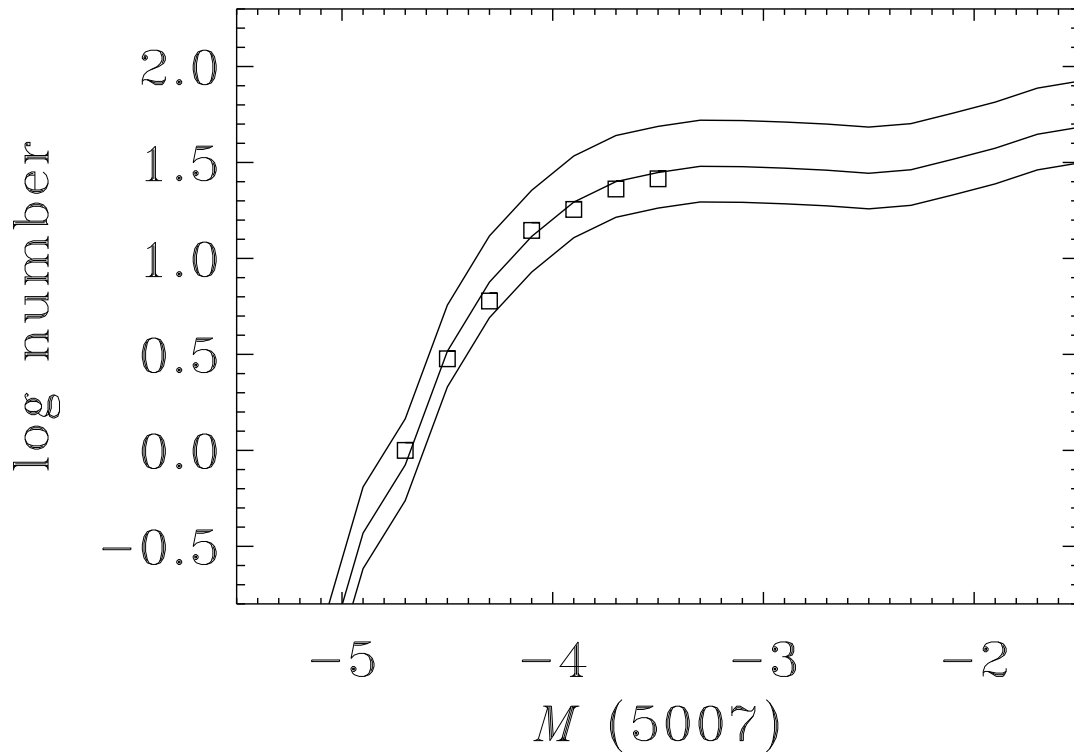


Fig. 9.— Observed [O III]  $\lambda 5007$  PNLF of NGC 1344 (*squares*), with the 91 data from the statistically complete sample binned into 0.2 mag intervals. The apparent magnitudes  $m(5007)$  have been transformed into absolute magnitudes  $M(5007)$  by adopting an extinction correction of 0.066 mag and a distance modulus  $m - M = 31.38$ . The three lines are PNLF simulations (Méndez & Soffner 1997) for three different sample sizes: 1500, 2300, and 4000 PNs. From the sample size, it is possible to estimate the PN formation rate (see text).



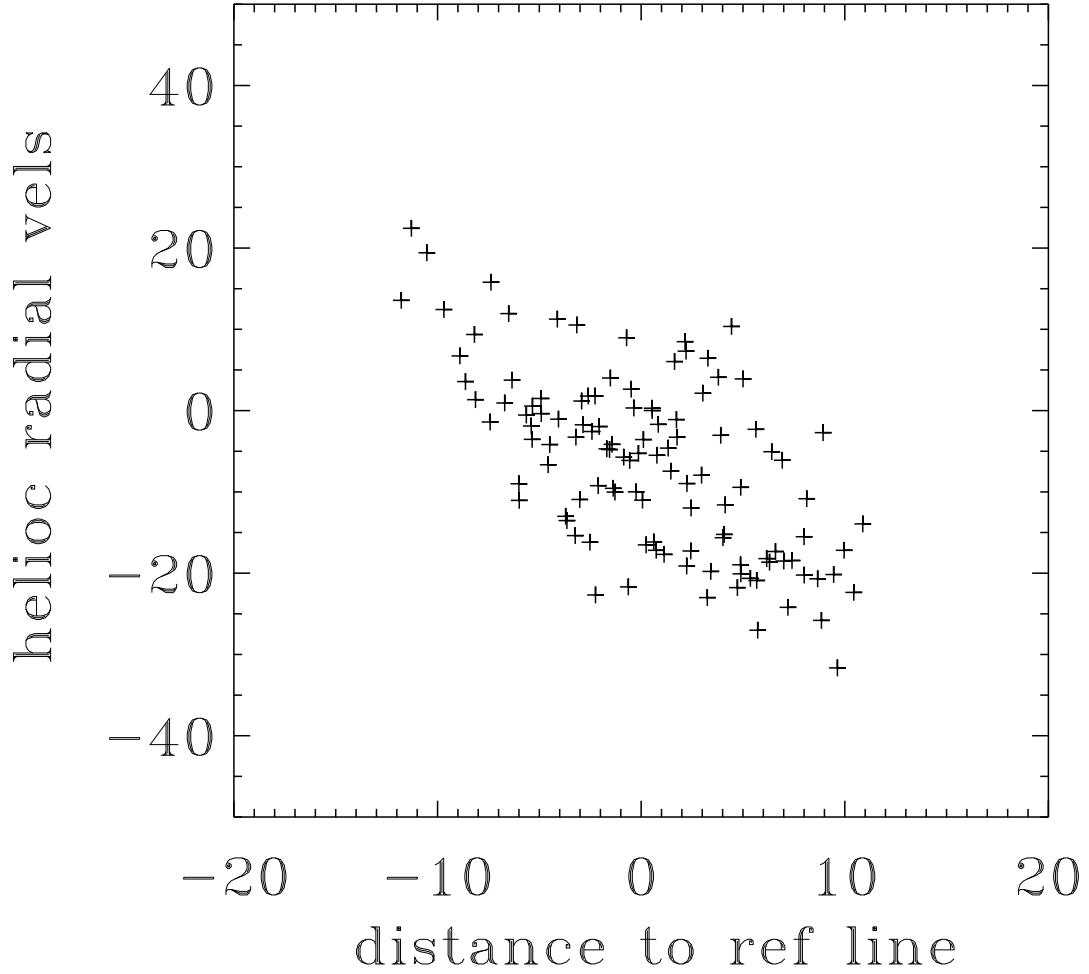


Fig. 10.— Slitless velocities of NGC 7293 measured at 114 undispersed positions. The velocities, in units of  $\text{km s}^{-1}$ , are plotted as a function of the distance from the undispersed position to a diagonal reference line. These distances, expressed in hundreds of pixels, are defined as positive above the reference line and negative below.

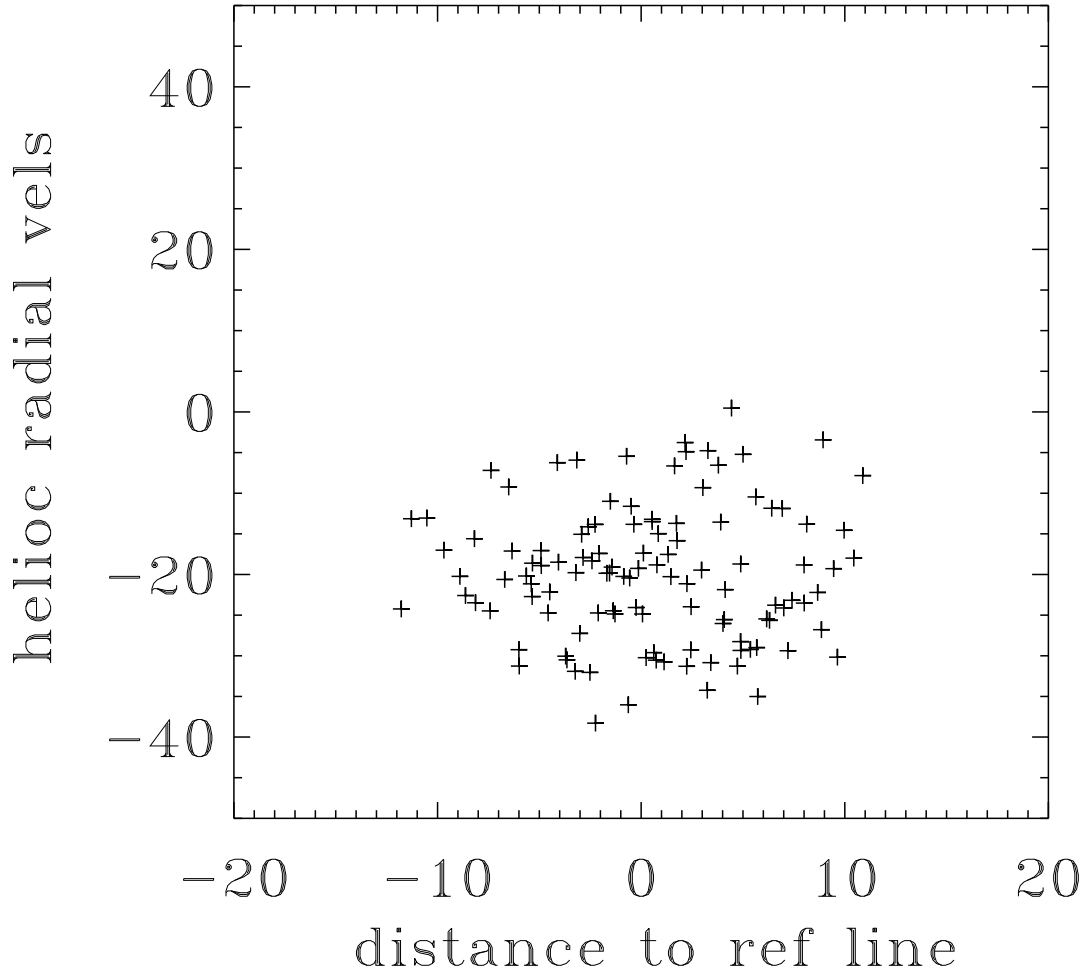


Fig. 11.— Velocities of NGC 7293 plotted in Fig. 10, corrected as described in the text. From this figure, we estimate that the calibration errors in slitless velocities are below  $20 \text{ km s}^{-1}$ .

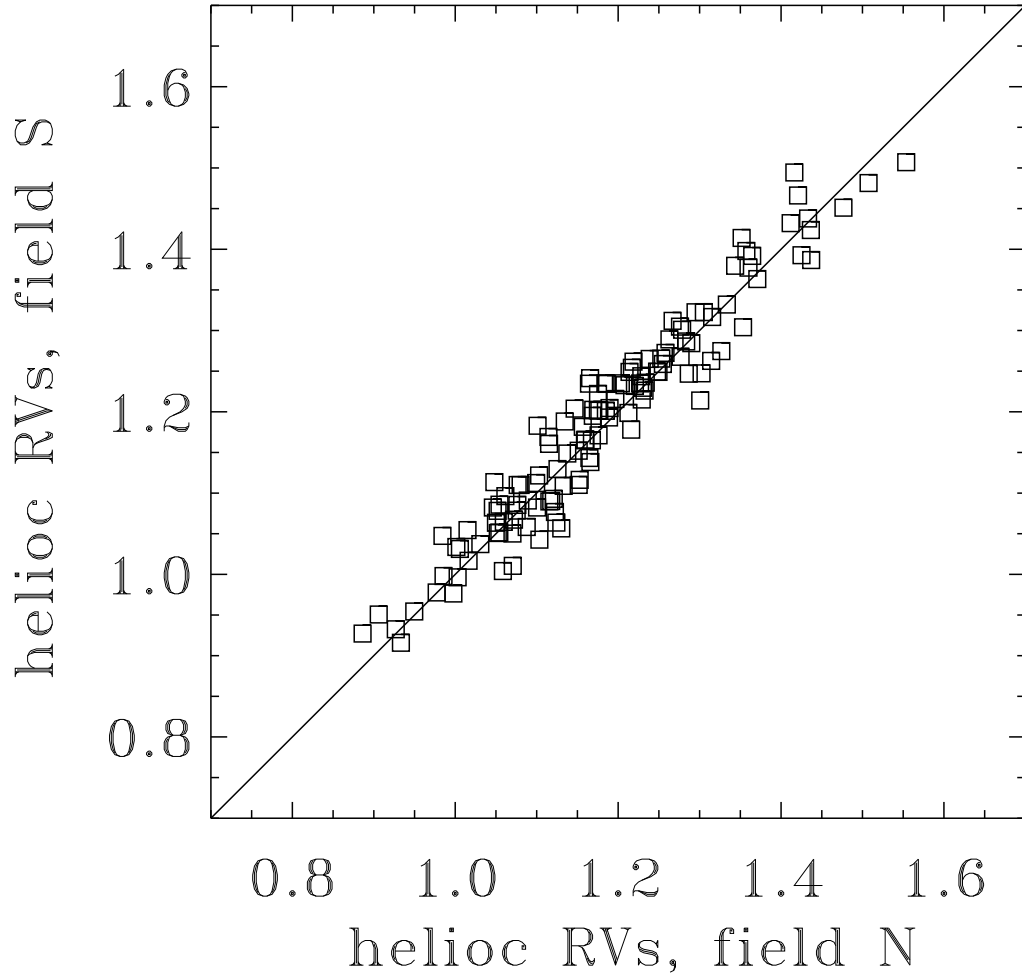


Fig. 12.— Velocities for 128 PNs measured in both N and S fields are compared (a few of the 132 objects shown in Fig. 8 could not be measured for velocities in both fields because the North grism images are too faint). The velocities are expressed in thousands of  $\text{km s}^{-1}$ . The standard deviation is  $34 \text{ km s}^{-1}$ .

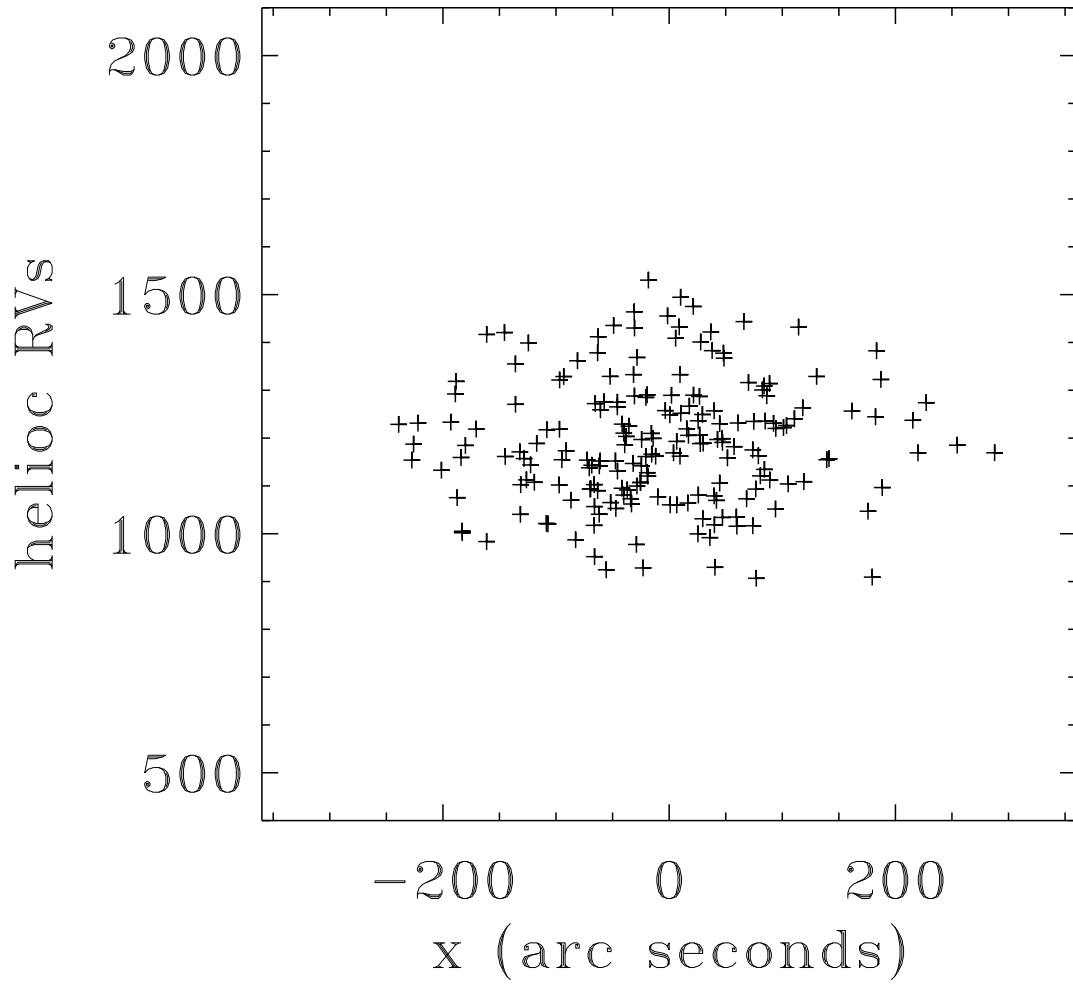


Fig. 13.— Velocities of the 195 PNs as a function of their  $x$  coordinates in arcseconds relative to the center of light of NGC 1344.

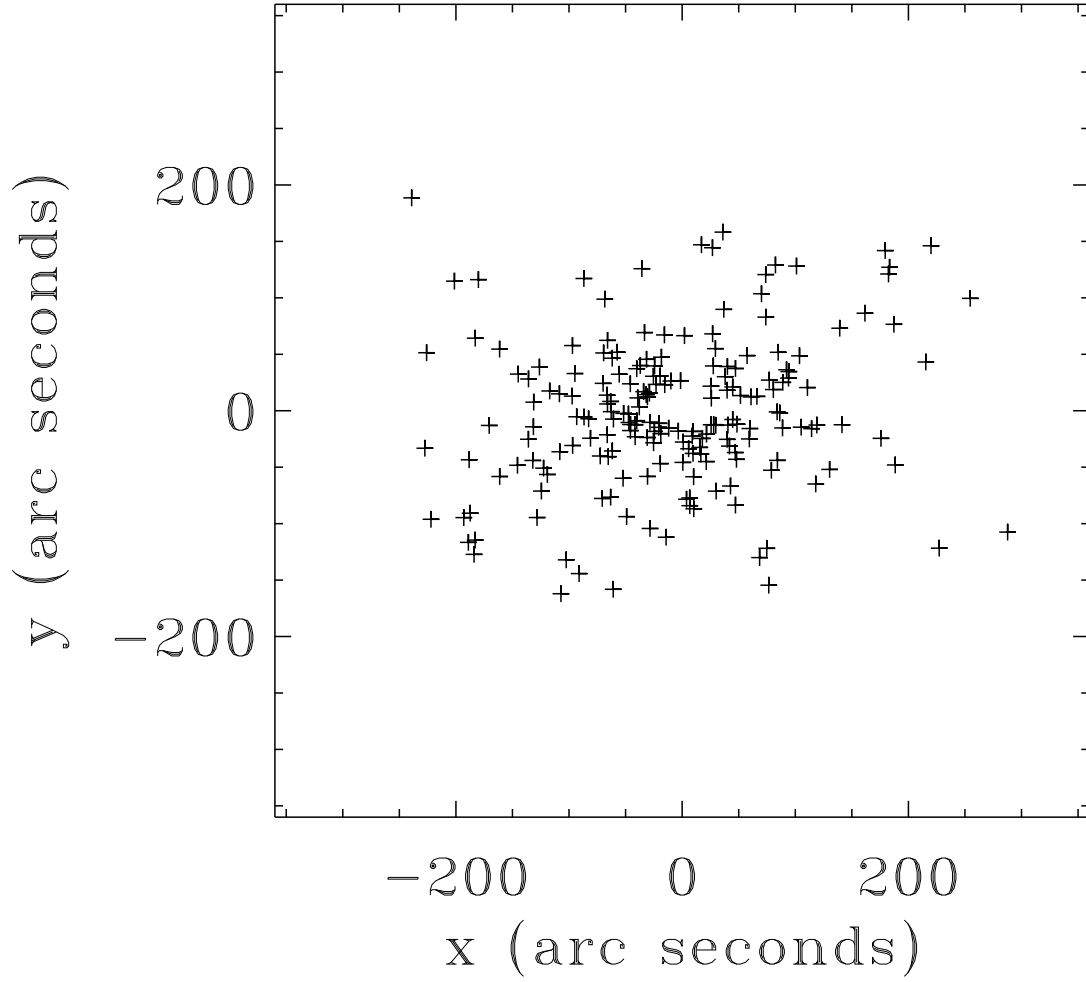


Fig. 14.— Positions of the 195 PNs in arcseconds relative to the center of light of NGC 1344. The  $x$  axis runs along the major axis,  $x$  coordinates are positive toward the south, and  $y$  coordinates are positive toward the east.

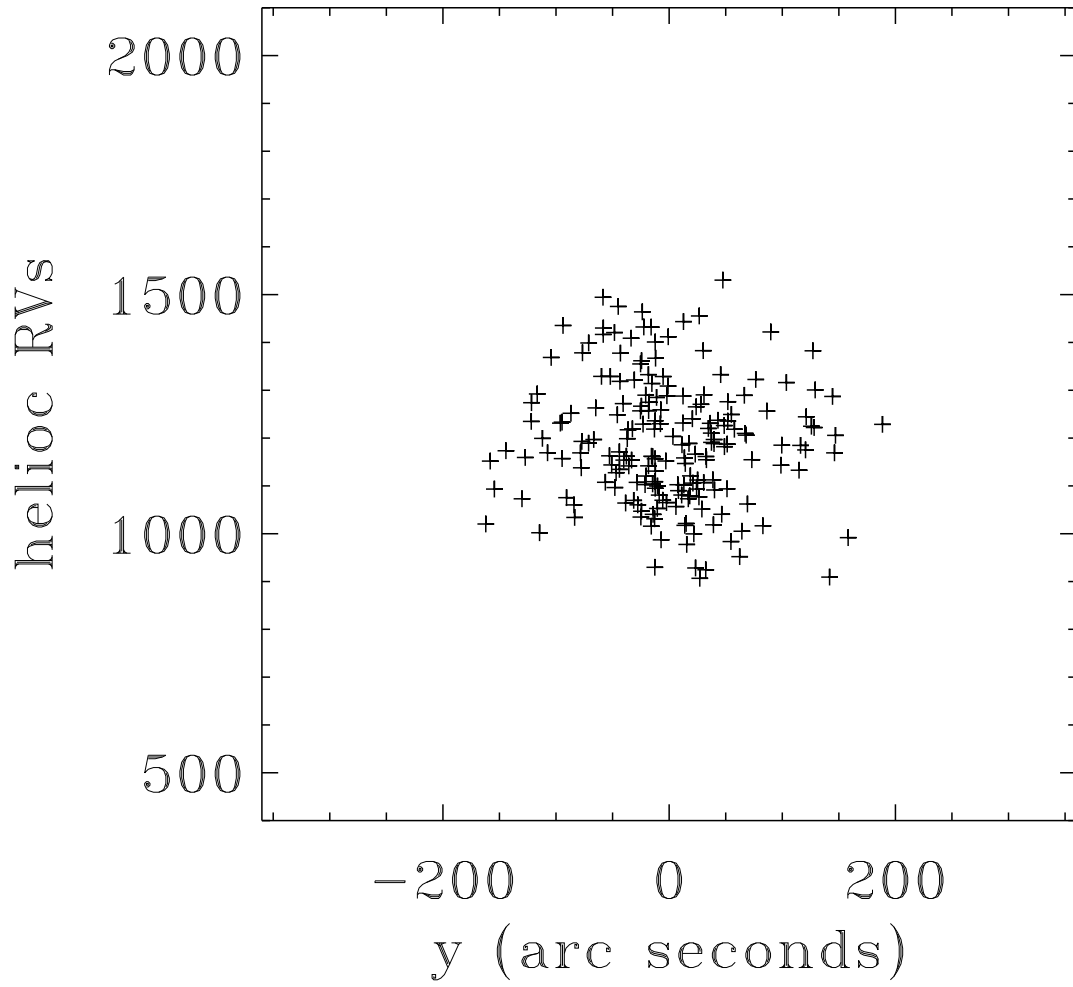


Fig. 15.— Velocities of the 195 PNs as a function of their  $y$  coordinates in arcseconds relative to the center of light of NGC 1344.

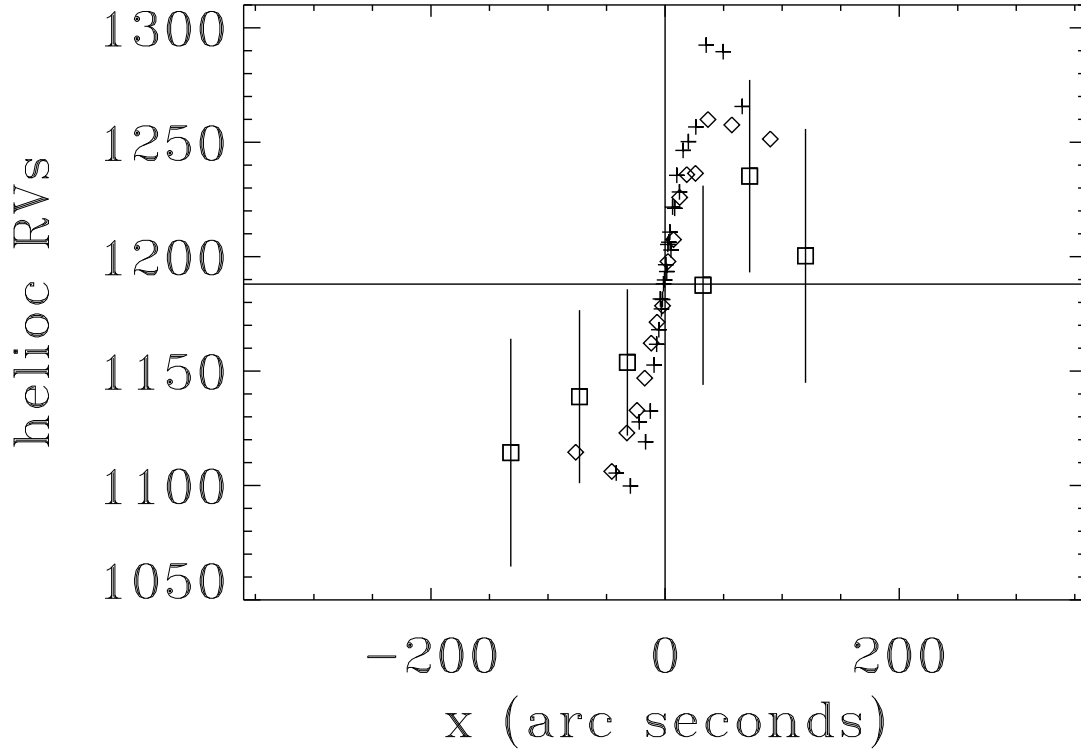


Fig. 16.— Velocities of PNs within  $\pm 20''$  of the x-axis. The selected PN velocities have been separated into six groups according to their x-coordinates. The squares with error bars indicate the average velocity within each group, plotted at the position of the average x-coordinate of the group. The numbers of PNs per group, from left to right, are 5, 10, 19, 8, 8, 4. The plus signs and diamonds represent velocities measured on our long-slit spectra along the major axis (see Fig. 1) and parallel to the major axis (see Fig. 3), respectively.

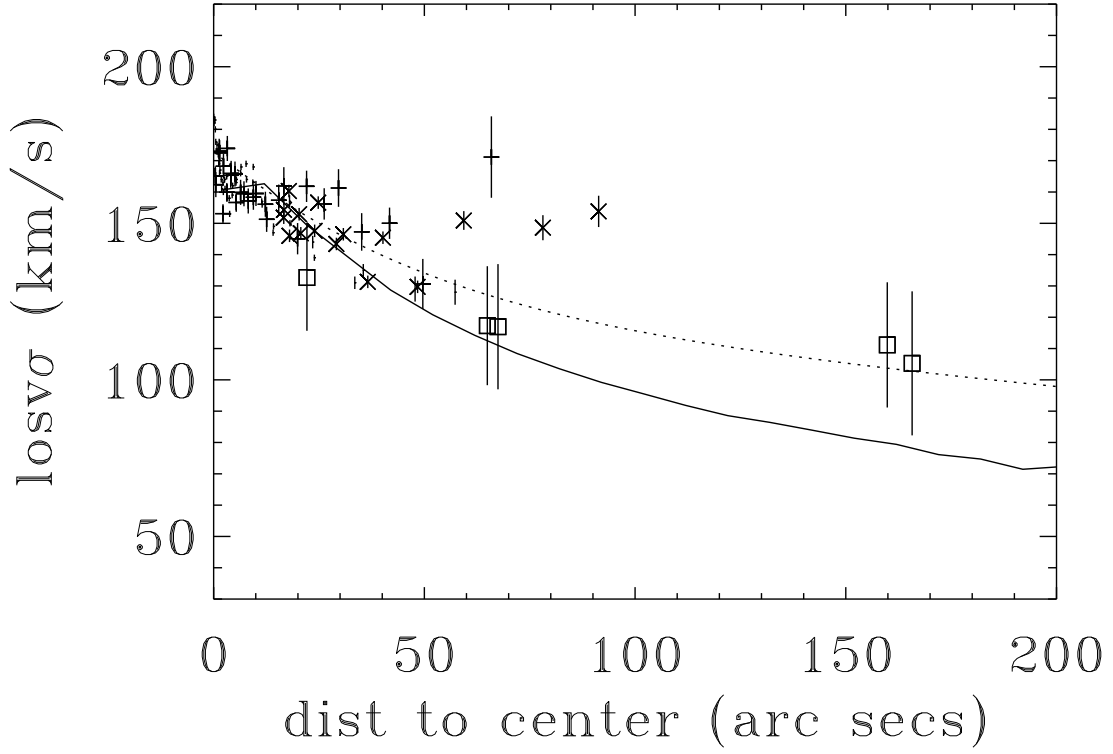


Fig. 17.— Squares with error bars are line-of-sight velocity dispersions from the PN velocities. The PNs have been separated into five groups according to projected angular distance from the center. The numbers of PNs per group are from north to south, passing through the center, 32, 40, 66, 35, 22. The vertical crosses represent dispersions measured on long-slit spectra along the major axis (see Fig. 1 and Table 1). The vertical segments are dispersions from Fig. 2 and Table 2. The asterisks are dispersions from Fig. 3 and Table 3. The vertical sizes of these 3 symbols represent the error bars. The solid line is the single-component analytical model of Hernquist (1990), with a constant M/L ratio and a total mass of  $1.5 \times 10^{11} M_{\odot}$ , adopting  $R_e = 46''$ . The dotted line is a two-component Hernquist model as described in the text; the second component is the dark matter halo.



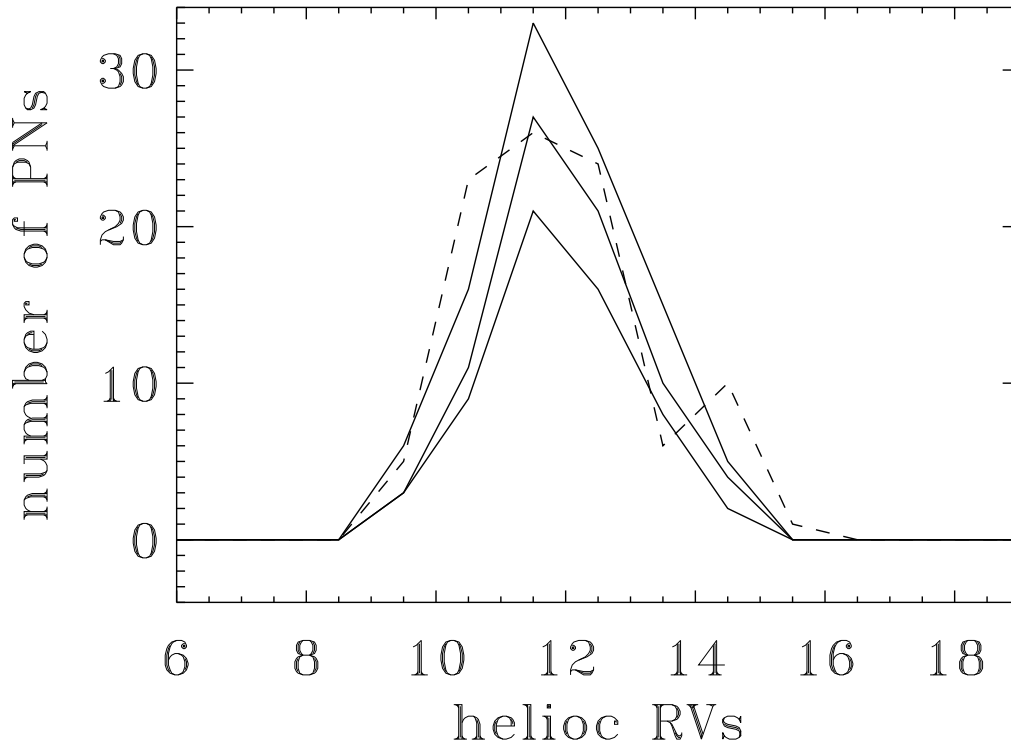


Fig. 18.— Graph showing the numbers of PNs as a function of velocity (expressed in hundreds of  $\text{km s}^{-1}$ ) at different angular distances from the center of NGC 1344. The bin size is  $100 \text{ km s}^{-1}$ . The solid lines give the numbers of PNs more distant than 80, 100, and  $120''$  from the center. The dashed line is for PNs closer than  $80''$  from the center. An excess of PNs moving in tangential orbits outside would produce a double-peaked or at least a flat-topped histogram (PNs moving either toward or away from us), which is not observed. In fact, the distribution close to the center appears to be slightly more flat-topped. Consequently, we do not expect anisotropy effects to invalidate our conclusion about a dark matter halo around this galaxy. We have also verified that the shape of the line-of-sight velocity dispersion outside does not change significantly if we restrict the sample to only those PNs with large x-coordinates in modulus, i.e., eliminating distant PNs near the minor axis. Rotation does not affect the in-out relation; if we restrict the sample to the receding or approaching half of the galaxy, both the solid and the dashed peak become slightly narrower.

Table 1. The kinematics of NGC 1344 along the major axis (P.A.=167°) from Ca triplet data <sup>a</sup>

R	V	dV	$\sigma$	$d\sigma$	$h_3$	$dh_3$	$h_4$	$dh_4$
-0.400	0.978	2.99	165.2	3.49	0.006	0.014	-0.045	0.013
-1.309	-0.702	3.39	173.0	3.97	0.027	0.016	-0.02	0.014
-2.220	-7.532	2.50	153.1	2.94	0.002	0.013	-0.044	0.015
-3.129	-11.640	2.91	159.9	3.20	0.000	0.014	-0.061	0.016
-4.040	-7.282	3.16	165.3	3.61	0.028	0.016	-0.039	0.016
-5.368	-20.750	2.23	156.7	2.88	0.067	0.013	-0.032	0.014
-7.191	-27.110	2.98	159.4	3.64	0.041	0.019	-0.027	0.013
-9.429	-36.190	3.52	158.3	4.01	0.068	0.024	-0.048	0.016
-12.580	-56.310	4.11	151.3	3.70	0.061	0.02	-0.049	0.022
-16.660	-69.750	5.28	161.9	6.18	0.071	0.022	0.002	0.019
-22.060	-61.030	6.11	161.8	5.36	0.036	0.026	-0.056	0.026
-29.620	-89.040	6.07	161.3	5.53	0.001	0.032	-0.086	0.021
-41.740	-83.400	7.35	150.0	4.96	0.110	0.044	-0.192	0.037
0.511	7.658	3.21	162.4	4.00	-0.001	0.015	-0.036	0.014
1.420	4.658	3.19	172.6	3.53	0.021	0.016	-0.036	0.014
2.330	16.530	3.78	168.2	3.47	-0.011	0.012	-0.053	0.014
3.240	17.490	4.27	173.9	3.87	-0.002	0.013	-0.03	0.014
4.150	21.920	3.94	165.9	4.32	-0.01	0.012	-0.009	0.013
5.061	14.060	4.70	165.7	4.93	-0.025	0.014	-0.023	0.016
6.398	32.820	3.91	159.9	2.81	-0.031	0.013	-0.044	0.019
8.213	32.320	3.62	157.1	2.40	-0.044	0.014	-0.074	0.018
10.030	46.720	4.70	159.5	3.33	-0.038	0.015	-0.057	0.021
12.270	39.470	4.64	156.1	3.50	-0.071	0.019	-0.041	0.023
15.430	57.620	4.42	157.4	4.71	-0.037	0.019	-0.037	0.022
19.920	61.450	4.57	145.1	4.84	-0.068	0.023	-0.017	0.024
26.230	67.880	5.25	156.2	5.10	-0.01	0.022	-0.082	0.028
35.120	103.600	6.52	147.2	5.50	-0.035	0.027	-0.011	0.024
49.630	100.800	8.72	130.6	7.56	-0.071	0.037	-0.021	0.031
65.910	76.820	20.19	171.2	13.00	0.031	0.081	-0.244	0.061

<sup>a</sup>Positive radii are to the east.

Table 2. The kinematics of NGC 1344 along the minor axis (P.A.=77°) <sup>a</sup>

R	V	dV	$\sigma$	$d\sigma$	$h_3$	$dh_3$	$h_4$	$dh_4$
-0.012	1.436	0.99	183.9	1.05	0.003	0.004	-0.001	0.004
-0.212	0.506	1.02	182.7	1.06	0.012	0.004	-0.012	0.004
-0.412	0.436	1.01	180.4	1.06	0.028	0.004	-0.012	0.004
-0.612	-1.784	0.95	172.6	1.02	0.015	0.004	-0.003	0.003
-0.812	0.686	1.00	175.3	1.07	-0.002	0.004	-0.004	0.004
-1.012	-0.674	1.10	173.4	1.21	0.001	0.005	0.005	0.004
-1.212	-3.924	1.06	168.9	1.14	-0.001	0.005	-0.012	0.004
-1.507	-0.314	0.79	166.9	0.89	0.010	0.003	0.010	0.003
-1.907	2.036	0.89	161.2	1.04	0.020	0.004	0.025	0.004
-2.307	2.256	0.99	159.9	1.13	-0.003	0.005	0.013	0.004
-2.708	4.006	1.07	160.9	1.23	0.004	0.005	0.020	0.005
-3.202	1.936	0.99	157.6	1.15	-0.027	0.005	0.020	0.004
-3.803	2.326	1.10	152.8	1.29	-0.025	0.006	0.023	0.005
-4.499	1.536	1.13	161.9	1.39	0.006	0.005	0.039	0.006
-5.394	2.466	1.07	163.9	1.22	0.017	0.005	0.009	0.004
-6.489	1.216	1.15	168.3	1.25	0.014	0.005	-0.006	0.004
-7.784	5.576	1.30	163.6	1.43	0.011	0.006	-0.008	0.005
-9.376	-0.894	1.27	167.6	1.31	-0.015	0.006	-0.032	0.005
-11.450	7.366	1.13	155.6	1.26	0.017	0.006	-0.010	0.004
-14.230	1.326	1.24	149.2	1.40	-0.004	0.006	-0.011	0.005
-17.950	2.576	1.40	156.8	1.58	-0.009	0.006	0.005	0.005
-23.510	10.480	1.46	143.7	1.63	-0.001	0.008	-0.017	0.006
-33.500	11.440	1.62	131.3	1.81	0.022	0.009	-0.026	0.008
-47.750	8.476	3.54	128.5	3.75	0.055	0.02	-0.047	0.015
0.188	-1.494	0.97	181.6	1.00	0.008	0.004	-0.011	0.004
0.388	0.756	0.97	183.4	1.00	0.007	0.004	-0.012	0.004
0.588	-0.394	0.91	176.3	0.99	0.008	0.004	0.000	0.003
0.788	-1.714	0.98	173.4	1.09	0.006	0.004	0.007	0.004
0.988	0.326	1.05	172.5	1.15	0.008	0.004	0.001	0.004
1.188	-1.424	1.10	171.6	1.24	-0.004	0.005	0.020	0.004
1.483	2.506	0.78	165.8	0.88	-0.001	0.004	0.006	0.003

Table 2—Continued

R	V	dV	$\sigma$	$d\sigma$	$h_3$	$dh_3$	$h_4$	$dh_4$
1.884	0.786	0.94	163.5	1.05	-0.009	0.004	-0.001	0.004
2.284	-0.464	1.01	162.9	1.14	-0.013	0.005	0.002	0.004
2.684	-4.284	1.14	163.6	1.29	0.002	0.005	0.006	0.004
3.178	-5.144	1.00	164.8	1.13	0.008	0.004	0.005	0.004
3.780	-1.464	1.10	157.8	1.26	0.011	0.005	0.017	0.005
4.474	-1.314	1.07	159.4	1.23	-0.004	0.005	0.019	0.005
5.371	0.936	1.10	162.9	1.27	-0.020	0.005	0.020	0.005
6.466	-5.574	1.21	165.6	1.37	0.007	0.005	0.006	0.004
7.762	14.200	1.26	168.6	1.36	0.005	0.005	-0.011	0.004
9.351	3.216	1.25	163.2	1.36	0.044	0.006	-0.016	0.005
11.430	-4.324	1.24	157.1	1.37	0.015	0.006	-0.010	0.005
14.200	-5.254	1.34	147.3	1.54	-0.011	0.007	0.000	0.006
18.020	-17.180	0.89	150.3	1.18	0.017	0.008	-0.029	0.005
23.910	-17.290	1.05	139.2	1.34	-0.030	0.009	-0.020	0.005
35.450	-12.790	1.92	135.3	2.22	0.021	0.01	-0.002	0.009
57.330	-3.104	4.70	127.7	3.65	-0.017	0.029	-0.205	0.029

<sup>a</sup>Positive radii are to the east.

Table 3. The kinematics of NGC 1344 parallel to the major axis (P.A.=167°) <sup>a</sup>

R	D	V	dV	$\sigma$	$d\sigma$	$h_3$	$dh_3$	$h_4$	$dh_4$
-2.156	16.64	-9.461	0.96	151.8	1.32	0.032	0.008	-0.022	0.005
-6.843	17.86	-16.610	1.01	160.3	1.37	0.020	0.008	-0.001	0.005
-11.810	20.29	-25.800	1.18	152.9	1.59	0.049	0.008	-0.015	0.006
-17.370	23.96	-41.060	1.15	147.6	1.52	0.015	0.008	-0.030	0.006
-24.000	29.13	-55.140	1.14	143.4	1.16	0.056	0.008	-0.030	0.007
-32.640	36.57	-65.040	1.17	131.3	1.29	0.030	0.008	-0.011	0.007
-45.500	48.40	-81.830	1.46	129.7	1.6	0.097	0.011	0.025	0.009
-76.360	78.13	-73.470	3.18	148.6	3.53	0.053	0.018	-0.026	0.015
2.425	16.68	9.869	1.45	154.3	1.6	-0.015	0.007	-0.015	0.005
7.192	18.00	19.450	1.40	146.0	1.57	0.004	0.007	-0.007	0.006
12.470	20.68	37.890	1.35	146.8	1.51	-0.017	0.007	-0.011	0.006
18.540	24.82	47.860	1.58	156.6	1.66	-0.017	0.008	-0.013	0.006
25.980	30.77	48.400	1.62	146.5	1.78	-0.016	0.008	0.001	0.006
36.630	40.18	71.950	1.21	145.4	2.1	-0.013	0.008	-0.023	0.008
57.020	59.36	69.590	2.87	150.9	2.86	0.028	0.014	-0.037	0.01
89.850	91.35	63.410	5.77	153.8	4.98	0.066	0.028	-0.117	0.019

<sup>a</sup>The long slit was located parallel to the major axis and shifted 16.5 arcsec to the northeast. Radii R give the distance in arcsec from the minor axis and are positive to the east; the corresponding distances D from the center are also given.

Table 4. PN Observations and calibrations

Field	Config	FORS1 CCD frame identification	exp (s)	Air mass <sup>a</sup>
LTT 9491	on-band	FORS1.2001-09-22T04:05:22:194.fits	30	1.01
NGC 7293 p1	on-band	FORS1.2001-09-22T04:27:47:215.fits	100	1.05
NGC 7293 p1	grism+on	FORS1.2001-09-22T04:32:04:729.fits	250	1.05
NGC 7293 p2	on-band	FORS1.2001-09-22T04:48:42:887.fits	100	1.09
NGC 7293 p2	grism+on	FORS1.2001-09-22T04:53:28:250.fits	250	1.10
NGC 7293 p3	on-band	FORS1.2001-09-22T05:04:43:352.fits	100	1.12
NGC 7293 p3	grism+on	FORS1.2001-09-22T05:08:52:999.fits	250	1.13
NGC 7293 p4	on-band	FORS1.2001-09-22T05:20:03:180.fits	100	1.16
NGC 7293 p4	grism+on	FORS1.2001-09-22T05:24:04:002.fits	250	1.18
NGC 7293 p5	on-band	FORS1.2001-09-22T05:35:00:380.fits	100	1.20
NGC 7293 p5	grism+on	FORS1.2001-09-22T05:40:37:185.fits	250	1.23
NGC 7293 p6	on-band	FORS1.2001-09-22T05:52:04:241.fits	100	1.27
NGC 7293 p6	grism+on	FORS1.2001-09-22T05:56:25:585.fits	250	1.29
NGC 1344 S	off-band	FORS1.2001-09-22T06:17:30:081.fits	900	1.1
NGC 1344 S	on-band	FORS1.2001-09-22T06:41:51:834.fits	1500	1.06
NGC 1344 S	grism+on	FORS1.2001-09-22T07:08:58:932.fits	2400	1.03
NGC 1344 S	off-band	FORS1.2001-09-22T07:55:35:179.fits	900	1.01
NGC 1344 S	on-band	FORS1.2001-09-22T08:17:36:345.fits	1500	1.01
NGC 1344 S	grism+on	FORS1.2001-09-22T08:44:51:873.fits	1827	1.02
MOS cal. p1	disp.	FORS1.2001-09-22T14:08:49:563.fits	300	–
MOS cal. p1	undisp.	FORS1.2001-09-22T14:17:03:080.fits	10	–
MOS cal. p2	disp.	FORS1.2001-09-22T14:52:19:858.fits	300	–
MOS cal. p2	undisp.	FORS1.2001-09-22T15:00:33:521.fits	10	–
MOS cal. p3	disp.	FORS1.2001-09-22T15:38:12:124.fits	300	–
MOS cal. p3	undisp.	FORS1.2001-09-22T15:46:25:584.fits	10	–
MOS cal. p4	disp.	FORS1.2001-09-22T16:23:22:833.fits	300	–
MOS cal. p4	undisp.	FORS1.2001-09-22T16:31:36:609.fits	10	–
MOS cal. p5	disp.	FORS1.2001-09-22T17:06:49:582.fits	300	–
MOS cal. p5	undisp.	FORS1.2001-09-22T17:15:03:150.fits	10	–
MOS cal. p6	disp.	FORS1.2001-09-22T18:13:33:890.fits	300	–
MOS cal. p6	undisp.	FORS1.2001-09-22T18:21:47:136.fits	10	–

Table 4—Continued

Field	Config	FORS1 CCD frame identification	exp (s)	Air mass <sup>a</sup>
MOS cal. p7	disp.	FORS1.2001-09-22T18:59:11:971.fits	300	–
MOS cal. p7	undisp.	FORS1.2001-09-22T19:07:24:599.fits	10	–
MOS cal. p8	disp.	FORS1.2001-09-22T19:43:11:971.fits	300	–
MOS cal. p8	undisp.	FORS1.2001-09-22T19:51:25:471.fits	10	–
MOS cal. p9	disp.	FORS1.2001-09-22T20:26:26:536.fits	300	–
MOS cal. p9	undisp.	FORS1.2001-09-22T20:34:40:031.fits	10	–
NGC 1344 S	off-band	FORS1.2001-09-23T04:26:37:276.fits	900	1.48
NGC 1344 S	on-band	FORS1.2001-09-23T04:47:53:785.fits	1500	1.36
NGC 1344 S	grism+on	FORS1.2001-09-23T05:15:01:342.fits	2400	1.25
NGC 1344 N	off-band	FORS1.2001-09-23T06:02:09:802.fits	900	1.12
NGC 1344 N	on-band	FORS1.2001-09-23T06:24:03:346.fits	1500	1.08
NGC 1344 N	grism+on	FORS1.2001-09-23T06:51:11:402.fits	2400	1.04
NGC 1344 N	off-band	FORS1.2001-09-23T07:38:42:634.fits	900	1.01
NGC 1344 N	on-band	FORS1.2001-09-23T08:02:08:717.fits	1500	1.01
NGC 1344 N	grism+on	FORS1.2001-09-23T08:29:25:128.fits	2400	1.01
MOS cal. p10	disp.	FORS1.2001-09-23T14:03:18:215.fits	300	–
MOS cal. p10	undisp.	FORS1.2001-09-23T14:11:31:684.fits	10	–
LTT 9491	on-band	FORS1.2001-09-24T04:06:24:483.fits	30	1.01
NGC 1344 S	off-band	FORS1.2001-09-24T04:27:23:025.fits	900	1.45
NGC 1344 S	on-band	FORS1.2001-09-24T04:49:35:559.fits	1500	1.34
NGC 1344 S	grism+on	FORS1.2001-09-23T05:16:52:419.fits	2400	1.23
NGC 1344 N	off-band	FORS1.2001-09-24T06:03:08:777.fits	900	1.11
NGC 1344 N	on-band	FORS1.2001-09-24T06:25:31:046.fits	1500	1.07
NGC 1344 N	grism+on	FORS1.2001-09-24T06:52:47:665.fits	2400	1.04
NGC 1344 N	off-band	FORS1.2001-09-24T07:39:13:468.fits	900	1.01
NGC 1344 N	on-band	FORS1.2001-09-24T08:00:32:362.fits	1500	1.01
NGC 1344 N	grism+on	FORS1.2001-09-24T08:27:49:243.fits	2400	1.01



<sup>a</sup>The air masses correspond to the middle of each exposure.

Table 5. Detected Objects <sup>a</sup>

x,N	y,N	x,S	y,S	x,G	y,G	$\alpha$	(2000)	$\delta$	(2000)	m(5007)	Helioc. RV		
1772.260	1067.358	1729.156	2022.205	-535.833	-810.471	3	28	5.2512	-31	3	3.5266	27.937	1020.311
1632.203	1466.408	—	—	-919.991	-635.988	3	28	6.3293	-31	1	40.0443	28.370	1159.411
1732.279	839.470	1689.801	1793.004	-304.701	-790.873	3	28	6.4752	-31	3	47.1973	27.564	1151.846
1675.807	996.393	1634.140	1948.803	-455.580	-721.392	3	28	6.9138	-31	3	14.4031	28.350	1173.469
1581.728	1495.769	—	—	-944.840	-583.151	3	28	7.0245	-31	1	32.5186	27.791	1292.323
1568.797	1466.721	—	—	-914.774	-572.802	3	28	7.3000	-31	1	37.7783	27.896	1001.945
—	—	1577.605	2010.898	-512.529	-660.659	3	28	7.6005	-31	3	0.3268	28.621	—
1494.271	1669.559	—	—	-1110.346	-480.877	3	28	7.8965	-31	0	55.1857	27.412	1231.241
1474.310	1525.730	—	—	-965.324	-473.528	3	28	8.5927	-31	1	22.8712	27.224	1233.207
1451.916	1499.147	—	—	-936.894	-453.540	3	28	9.0072	-31	1	27.3344	28.064	1075.390
1655.629	156.423	1610.347	1109.954	382.551	-772.650	3	28	9.5162	-31	5	59.2049	27.700	1093.308
1445.544	1203.287	—	—	-641.604	-472.970	3	28	9.9023	-31	2	25.4384	27.901	1157.112
1482.401	626.818	1439.235	1580.290	-71.019	-560.140	3	28	10.8886	-31	4	20.4240	27.865	1199.380
1450.042	700.912	1407.126	1654.197	-141.928	-521.579	3	28	11.1839	-31	4	4.6930	27.754	1368.677
1537.370	206.778	1492.272	1160.932	342.377	-650.516	3	28	11.1916	-31	5	45.0943	27.866	1073.010
1406.876	808.542	1363.645	1762.050	-245.484	-469.030	3	28	11.5590	-31	3	41.9376	27.439	1435.532
1327.086	1194.226	—	—	-622.254	-355.761	3	28	11.7452	-31	2	23.0969	27.405	1398.835
1492.896	179.792	1449.194	1132.072	374.009	-609.341	3	28	11.9401	-31	5	49.0562	27.987	1234.882
1279.115	1383.261	—	—	-806.383	-291.488	3	28	11.9718	-31	1	44.1504	27.447	1416.750
1336.050	923.200	1292.807	1875.584	-352.972	-388.523	3	28	12.3383	-31	3	16.9917	27.438	1137.857
1182.850	1723.840	—	—	-1137.278	-165.911	3	28	12.5280	-31	0	33.6594	27.734	1153.978
1216.906	1524.225	—	—	-941.386	-217.239	3	28	12.5443	-31	1	14.1989	27.882	1318.683
1327.977	886.447	1283.499	1839.981	-316.174	-383.019	3	28	12.5684	-31	3	23.8307	28.141	1378.188
1251.514	1174.306	—	—	-595.823	-282.204	3	28	12.9571	-31	2	24.3947	27.695	1107.595
1222.528	1309.240	—	—	-727.714	-241.575	3	28	13.0387	-31	1	56.7847	27.941	1420.634
1346.470	516.127	1302.970	1468.940	51.441	-434.236	3	28	13.2772	-31	4	37.5627	27.789	1251.879
1225.027	1193.297	—	—	-612.433	-254.170	3	28	13.3125	-31	2	19.7530	28.306	1143.868
1334.318	535.238	1291.310	1487.350	33.790	-420.740	3	28	13.4086	-31	4	33.4566	27.458	1060.261
1195.220	1243.830	—	—	-660.172	-220.070	3	28	13.6343	-31	2	8.7392	27.739	1171.125
1307.240	551.810	1263.258	1504.515	19.388	-391.810	3	28	13.7880	-31	4	29.1719	27.171	1169.060
1300.053	538.611	1256.637	1490.771	33.410	-386.106	3	28	13.9295	-31	4	31.5820	27.986	1193.068
1239.020	839.470	—	—	-261.169	-298.945	3	28	14.0540	-31	3	29.9899	28.199	1329.094
1314.171	333.836	1270.505	1287.251	235.561	-417.838	3	28	14.2660	-31	5	12.3344	27.855	1033.992
1221.654	732.392	1178.050	1685.052	-153.042	-291.001	3	28	14.6093	-31	3	50.5824	27.648	1430.127
1146.539	1128.379	—	—	-540.919	-181.637	3	28	14.6926	-31	2	29.7986	27.186	1217.258
1260.400	423.824	1216.438	1377.827	150.322	-356.256	3	28	14.8462	-31	4	52.6414	27.693	1189.185
1103.586	1271.259	—	—	-679.512	-126.398	3	28	14.9664	-31	2	0.1286	27.971	1355.132
—	—	1382.000	373.000	1136.185	-608.551	3	28	15.0094	-31	8	16.5477	28.548	1273.989
1149.584	948.411	1106.460	1901.321	-362.103	-200.606	3	28	15.1321	-31	3	5.4698	27.628	1153.914
1057.609	1449.172	—	—	-852.738	-65.087	3	28	15.1921	-31	1	23.4480	27.872	1218.677
1149.064	913.433	1106.338	1865.588	-326.854	-203.368	3	28	15.2307	-31	3	12.4187	27.802	1272.135
1114.081	1074.355	—	—	-484.266	-154.010	3	28	15.3363	-31	2	39.3361	28.136	1321.446
1204.960	528.929	1162.060	1482.319	50.708	-292.422	3	28	15.4102	-31	4	30.0714	27.401	1494.460
1231.899	363.259	1188.650	1316.010	213.733	-333.552	3	28	15.4436	-31	5	3.7308	27.733	1197.022
1122.577	896.442	1079.598	1850.976	-308.793	-178.233	3	28	15.6814	-31	3	14.6159	28.088	1141.782
1160.184	681.417	1116.790	1633.952	-96.850	-234.318	3	28	15.6882	-31	3	58.4995	27.468	1127.564
1046.614	1254.267	—	—	-657.621	-71.115	3	28	15.8857	-31	2	1.5019	28.189	1040.462
1075.186	997.640	1031.834	1951.217	-404.983	-122.058	3	28	16.1397	-31	2	53.0896	26.959	1361.660
1146.066	582.595	1103.000	1535.130	2.812	-229.030	3	28	16.1689	-31	4	17.5470	27.669	1248.618
—	—	1089.688	1431.980	106.711	-225.057	3	28	16.6486	-31	4	37.4872	27.766	1475.259
1053.000	925.500	1010.000	1878.600	-330.961	-106.440	3	28	16.6727	-31	3	6.5890	27.229	1102.650

Table 5—Continued

x,N	y,N	x,S	y,S	x,G	y,G	$\alpha$	(2000)	$\delta$	(2000)	m(5007)	Helioc. RV		
1102.462	540.615	1058.921	1494.332	47.865	-188.962	3	28	16.9534	-31	4	24.1319	28.072	1162.075
1070.703	718.529	1027.624	1672.063	-126.533	-142.056	3	28	16.9611	-31	3	47.9869	27.891	1107.360
1051.112	802.488	1007.918	1754.601	-207.753	-115.227	3	28	17.0350	-31	3	30.8894	27.078	1229.233
1102.587	505.632	1059.608	1459.167	82.770	-192.424	3	28	17.0427	-31	4	31.0808	27.526	1064.190
—	—	1146.441	941.540	590.339	-324.336	3	28	17.0976	-31	6	16.1993	27.815	1263.080
1083.346	561.975	1040.492	1514.760	28.686	-168.440	3	28	17.1861	-31	4	19.3803	27.407	1408.857
1050.050	748.951	1006.509	1701.299	-154.429	-118.652	3	28	17.1980	-31	3	41.4020	27.849	1463.896
1147.065	189.787	1102.962	1141.947	394.270	-263.760	3	28	17.2204	-31	5	35.0143	27.681	1162.838
—	—	1284.873	77.850	1438.677	-537.514	3	28	17.2941	-31	9	11.3763	27.832	1169.158
985.144	1067.358	942.665	2019.893	-466.107	-26.762	3	28	17.3284	-31	2	36.3148	27.734	1328.693
1112.119	347.472	1068.134	1300.150	239.968	-215.240	3	28	17.3302	-31	5	2.6527	27.201	1377.647
1025.624	825.476	982.816	1778.275	-228.790	-87.994	3	28	17.3593	-31	3	25.3825	27.805	1274.882
990.142	1013.385	946.486	1967.297	-413.409	-35.799	3	28	17.4049	-31	2	47.0059	27.381	987.100
984.145	1034.374	940.945	1988.016	-433.681	-28.235	3	28	17.4367	-31	2	42.6869	27.481	1070.061
1073.516	513.931	1029.483	1466.333	77.646	-162.264	3	28	17.4760	-31	4	28.5608	27.040	1219.177
937.667	1262.263	—	—	-656.085	38.110	3	28	17.5344	-31	1	56.1392	27.504	1102.513
—	—	1012.630	1541.130	4.693	-138.777	3	28	17.5388	-31	4	13.2623	27.848	1060.297
1027.624	690.542	984.645	1643.077	-94.405	-101.673	3	28	17.6950	-31	3	52.1274	27.668	1120.551
1020.127	719.428	976.648	1672.063	-122.556	-91.434	3	28	17.7354	-31	3	46.1192	27.522	1141.971
1082.472	355.263	1038.743	1308.392	234.554	-185.135	3	28	17.7619	-31	5	0.0572	27.306	1198.642
998.638	827.475	956.033	1780.510	-228.556	-61.028	3	28	17.7697	-31	3	24.0504	27.932	1130.850
981.695	904.442	938.283	1857.818	-303.888	-37.024	3	28	17.8271	-31	3	8.2095	27.392	1259.208
998.138	807.485	954.659	1761.020	-208.810	-61.815	3	28	17.8349	-31	3	27.9369	27.458	1095.085
990.642	835.471	947.850	1788.069	-235.599	-52.291	3	28	17.8727	-31	3	22.2102	27.500	1052.846
1100.213	166.668	1057.609	1119.578	420.946	-219.815	3	28	17.9902	-31	5	37.9326	27.956	1134.524
1001.136	701.537	956.658	1655.071	-103.482	-73.538	3	28	18.0821	-31	3	48.8864	27.467	1161.269
1056.359	383.187	1012.693	1336.000	209.167	-156.733	3	28	18.0890	-31	4	53.6852	27.138	1069.719
—	—	982.622	1503.491	44.805	-112.164	3	28	18.1009	-31	4	19.6687	26.610	1432.312
1032.621	504.633	989.642	1459.167	89.365	-122.767	3	28	18.1173	-31	4	28.7393	27.397	1266.754
980.053	800.926	935.950	1754.273	-200.579	-44.068	3	28	18.1344	-31	3	28.5823	27.734	1080.764
1009.507	614.080	967.153	1567.114	-16.931	-90.579	3	28	18.1748	-31	4	6.4920	27.257	1257.332
1000.637	657.558	957.658	1611.093	-59.693	-77.620	3	28	18.1970	-31	3	57.5656	27.224	1162.000
981.928	742.383	938.983	1695.871	-142.542	-51.609	3	28	18.2546	-31	3	40.2141	27.260	1099.567
949.662	917.431	906.433	1869.966	-313.625	-4.109	3	28	18.2829	-31	3	4.6458	27.801	1411.818
—	—	1076.974	886.004	651.718	-259.970	3	28	18.3121	-31	6	24.7343	27.907	1328.860
982.707	702.034	939.666	1656.071	-102.684	-55.829	3	28	18.3549	-31	3	48.1654	26.895	1285.089
952.910	860.959	908.994	1815.560	-258.650	-11.834	3	28	18.3885	-31	3	15.6940	27.486	1065.086
1005.634	549.611	961.656	1502.146	47.950	-91.552	3	28	18.4220	-31	4	19.1263	27.502	1332.716
953.160	840.469	911.055	1793.379	-237.497	-14.845	3	28	18.4297	-31	3	19.9100	27.948	1152.034
1012.100	489.090	968.870	1441.900	107.507	-103.629	3	28	18.4769	-31	4	31.2593	26.671	1289.706
1027.124	395.686	983.645	1349.221	198.896	-126.581	3	28	18.4991	-31	4	50.1627	27.530	1256.861
891.190	1152.317	—	—	-542.513	74.828	3	28	18.5447	-31	2	16.1893	28.200	1021.353
882.195	1196.295	—	—	-585.541	87.622	3	28	18.5644	-31	2	7.2217	28.188	1188.734
896.188	1095.345	—	—	-486.185	64.883	3	28	18.6219	-31	2	27.6013	27.959	1101.874
917.177	936.422	873.699	1889.957	-330.200	30.075	3	28	18.7318	-31	2	59.6745	27.814	1056.746
1017.004	298.109	973.650	1251.768	296.917	-125.061	3	28	18.9164	-31	5	9.0248	27.972	1034.785
761.066	1752.893	—	—	-1129.456	256.800	3	28	18.9214	-31	0	13.2454	27.457	1187.350
904.684	923.429	861.705	1876.963	-316.189	41.140	3	28	18.9532	-31	3	1.7619	27.968	1089.950
837.716	1294.247	—	—	-679.242	140.468	3	28	18.9816	-31	1	46.3408	28.084	1270.676
918.427	795.491	874.698	1748.026	-189.405	16.628	3	28	19.0940	-31	3	27.5729	28.119	1203.448
819.725	1341.225	—	—	-724.465	162.485	3	28	19.1327	-31	1	36.4462	27.984	1161.518

Table 5—Continued

x,N	y,N	x,S	y,S	x,G	y,G	$\alpha$	(2000)	$\delta$	(2000)	m(5007)	Helioc. RV		
968.883	472.319	925.762	1424.985	128.048	-62.099	3	28	19.1858	-31	4	33.0927	26.685	1236.072
967.653	460.654	924.492	1414.246	139.316	-61.830	3	28	19.2365	-31	4	35.2556	27.216	1400.976
969.652	451.659	926.048	1404.314	148.589	-64.426	3	28	19.2365	-31	4	37.1645	27.484	1031.252
878.415	941.769	834.888	1894.368	-331.680	69.139	3	28	19.3128	-31	2	57.3331	27.431	1017.520
963.655	398.685	920.676	1350.220	202.415	-63.428	3	28	19.4657	-31	4	47.5328	27.684	929.716
971.151	299.733	927.110	1253.267	299.387	-78.904	3	28	19.6227	-31	5	7.0816	27.637	1015.795
879.508	805.798	834.843	1758.458	-196.302	56.769	3	28	19.6699	-31	3	24.1946	27.501	1185.988
957.158	358.704	913.331	1311.099	242.418	-59.981	3	28	19.6777	-31	4	55.0928	27.031	1367.070
—	—	1031.996	598.707	941.841	-240.211	3	28	19.7763	-31	7	19.8102	27.370	1096.552
869.701	765.006	827.846	1714.292	-153.253	61.437	3	28	19.9128	-31	3	32.2559	27.724	1287.923
937.667	379.002	893.731	1332.318	223.442	-38.701	3	28	19.9231	-31	4	50.3069	26.969	1229.942
780.744	1250.514	—	—	-630.703	193.411	3	28	19.9746	-31	1	53.0013	27.784	1112.564
827.721	963.409	784.742	1917.193	-349.433	121.305	3	28	20.0253	-31	2	51.2151	28.073	1093.367
—	—	817.601	1722.720	-159.208	71.336	3	28	20.0425	-31	3	30.6697	27.148	1146.783
795.612	1091.966	—	—	-474.062	164.782	3	28	20.1746	-31	2	24.7929	27.323	1154.685
848.711	781.498	805.732	1736.032	-170.417	84.573	3	28	20.1936	-31	3	27.7171	27.845	1072.999
853.209	756.210	810.667	1708.728	-144.633	77.583	3	28	20.1936	-31	3	33.0867	27.591	977.496
955.721	156.178	912.090	1110.020	443.570	-76.235	3	28	20.2416	-31	5	34.8701	27.880	1313.959
716.900	1432.980	—	—	-806.914	272.916	3	28	20.4622	-31	1	14.7688	27.876	983.573
819.546	844.139	776.094	1796.564	-229.207	119.230	3	28	20.4793	-31	3	14.5816	27.407	1265.305
945.164	74.843	901.860	1027.700	525.992	-73.013	3	28	20.6235	-31	5	50.6012	27.547	1104.052
—	—	904.309	981.020	572.112	-79.685	3	28	20.7076	-31	5	59.9670	27.740	1432.033
677.870	1544.290	—	—	-914.399	321.499	3	28	20.7600	-31	0	51.4778	27.539	1005.213
812.703	730.273	768.295	1682.974	-115.274	116.612	3	28	20.8974	-31	3	36.7191	27.502	928.356
781.244	896.442	738.140	1849.159	-278.133	161.785	3	28	20.9230	-31	3	2.9155	27.491	924.570
851.709	481.644	808.855	1434.054	129.087	55.298	3	28	20.9565	-31	4	27.1944	27.554	1080.868
810.230	691.542	766.751	1645.076	-76.930	115.273	3	28	21.0313	-31	3	44.2447	27.396	1166.348
—	—	886.068	959.094	595.544	-63.424	3	28	21.0450	-31	6	3.6749	28.160	1108.738
890.191	173.795	847.711	1128.328	431.337	-9.962	3	28	21.1917	-31	5	29.0405	27.833	1288.414
887.192	186.788	842.714	1139.323	419.737	-4.934	3	28	21.2209	-31	5	26.5205	28.200	1308.787
—	—	920.051	671.671	878.912	-122.329	3	28	21.2981	-31	7	1.5248	27.922	1047.020
791.864	665.929	747.885	1620.213	-50.166	131.619	3	28	21.3865	-31	3	48.5637	27.960	1076.886
777.290	744.960	734.250	1698.000	-127.047	152.503	3	28	21.3883	-31	3	32.6129	26.894	1106.965
—	—	875.307	848.722	706.434	-62.324	3	28	21.5085	-31	6	25.0571	27.352	1156.601
773.248	715.530	729.934	1668.561	-97.360	154.101	3	28	21.5350	-31	3	38.2709	27.635	1290.335
786.741	623.575	742.763	1577.109	-7.153	132.997	3	28	21.5806	-31	3	56.8103	27.004	1455.359
750.759	820.479	706.780	1775.013	-200.669	186.048	3	28	21.6003	-31	3	16.5935	27.721	1210.318
828.721	353.707	785.742	1307.742	257.736	67.181	3	28	21.6552	-31	4	51.4536	27.739	1158.525
830.845	306.855	787.866	1260.764	304.288	60.976	3	28	21.7462	-31	5	0.7782	28.120	1231.508
798.742	487.992	755.166	1440.623	127.301	108.986	3	28	21.7582	-31	4	24.0633	27.040	999.652
810.604	415.172	766.751	1368.211	198.619	90.978	3	28	21.7728	-31	4	38.7849	27.370	1078.912
713.277	932.424	670.798	1886.958	-308.987	232.397	3	28	21.8621	-31	2	53.2681	28.120	1040.566
735.128	806.846	691.444	1759.702	-184.903	200.211	3	28	21.8758	-31	3	18.9349	27.193	1091.364
826.722	280.742	782.743	1235.276	330.393	63.333	3	28	21.8904	-31	5	5.6740	27.770	1443.496
673.297	1113.336	—	—	-484.690	288.494	3	28	21.9934	-31	2	16.2991	27.861	1218.460
693.287	972.405	650.807	1926.939	-347.074	255.796	3	28	22.0603	-31	2	44.6988	27.927	1093.884
794.062	392.035	750.949	1344.766	223.230	105.058	3	28	22.0844	-31	4	42.8156	27.438	1105.837
731.304	743.657	688.134	1696.462	-121.618	198.255	3	28	22.1015	-31	3	31.2808	27.336	1197.023
685.087	913.304	641.538	1866.889	-286.964	259.305	3	28	22.3565	-31	2	56.1108	27.110	1276.030
705.531	781.868	661.427	1734.652	-157.386	227.725	3	28	22.4019	-31	3	22.8214	27.272	1332.696
751.883	428.670	708.284	1382.387	189.941	150.555	3	28	22.6362	-31	4	34.0334	27.816	1382.757

Table 5—Continued

x,N	y,N	x,S	y,S	x,G	y,G	$\alpha$	(2000)	$\delta$	(2000)	m(5007)	Helioc. RV		
789.865	211.646	746.280	1165.200	402.909	93.789	3	28	22.6362	-31	5	18.1297	27.278	1120.990
689.788	717.529	646.809	1670.064	-91.845	237.229	3	28	22.8078	-31	3	35.0299	28.140	1530.368
637.002	960.098	592.961	1914.320	-329.684	311.558	3	28	22.9710	-31	2	45.1314	28.419	952.023
709.279	490.275	664.926	1433.050	137.767	198.265	3	28	23.1452	-31	4	21.4677	27.605	1188.453
749.738	232.885	706.471	1186.695	385.107	135.467	3	28	23.1942	-31	5	12.5542	27.588	906.704
754.132	172.852	711.028	1126.075	444.814	125.750	3	28	23.2894	-31	5	24.5773	27.279	1112.274
705.899	423.095	662.432	1376.001	199.901	195.777	3	28	23.3572	-31	4	33.6008	26.805	1018.503
711.872	386.392	667.723	1340.068	235.590	187.001	3	28	23.3693	-31	4	40.9410	27.757	1190.921
768.251	61.849	724.000	1016.000	553.752	102.622	3	28	23.3778	-31	5	46.8590	28.083	1240.303
733.010	149.082	689.809	1102.727	470.128	144.787	3	28	23.6783	-31	5	28.4981	27.544	1051.541
704.904	150.281	661.052	1104.050	471.350	173.220	3	28	24.1074	-31	5	27.2415	27.467	1220.241
587.994	800.827	544.734	1754.205	-166.362	346.072	3	28	24.1460	-31	3	14.9730	27.022	1062.077
434.413	1658.190	—	—	-1006.647	573.956	3	28	24.1872	-31	0	20.5582	27.566	1132.798
697.347	160.676	654.181	1114.580	461.556	181.319	3	28	24.1914	-31	5	24.9687	27.641	1230.900
631.700	482.450	587.963	1436.048	146.906	275.031	3	28	24.3356	-31	4	19.2361	27.811	1249.315
591.087	712.282	547.233	1665.686	-78.410	335.571	3	28	24.3425	-31	3	32.5099	28.028	1209.823
650.121	340.367	606.422	1293.471	287.087	244.257	3	28	24.4370	-31	4	47.9654	26.723	1181.972
586.339	623.574	542.860	1577.109	10.292	332.388	3	28	24.6524	-31	3	49.8271	27.822	1289.374
418.421	1553.121	—	—	-900.583	580.730	3	28	24.7176	-31	0	40.7181	28.550	1184.626
623.071	204.654	580.314	1158.505	424.228	258.939	3	28	25.2103	-31	5	13.7009	27.499	1235.488
567.400	500.575	523.988	1453.824	134.613	340.489	3	28	25.2738	-31	4	13.4409	26.909	1206.170
630.942	109.196	587.162	1063.230	518.590	243.296	3	28	25.3537	-31	5	32.7827	27.861	1226.207
456.402	988.397	411.799	1942.306	-341.955	494.203	3	28	25.6704	-31	2	33.3211	28.358	1143.137
372.818	1089.035	—	—	-434.290	585.712	3	28	26.6686	-31	2	10.6412	27.929	—
455.153	460.400	411.549	1414.746	183.880	448.951	3	28	27.1062	-31	4	17.3616	27.404	1421.923
—	—	566.000	504.000	1076.802	215.762	3	28	27.1818	-31	7	22.2615	28.644	1237.231
473.020	272.616	429.900	1226.100	369.801	414.507	3	28	27.3338	-31	4	55.0928	28.010	1016.542
—	—	450.000	896.000	696.404	365.485	3	28	27.9096	-31	6	0.9009	28.419	1154.630
307.475	837.470	—	—	-177.987	628.881	3	28	28.3509	-31	2	57.9854	28.096	1224.732
371.319	300.670	328.540	1254.430	350.565	518.108	3	28	28.8144	-31	4	45.9810	27.796	1316.018
83.584	1878.457	—	—	-1195.502	942.648	3	28	28.9758	-30	59	24.8987	27.619	1228.745
—	—	412.000	659.000	935.814	382.685	3	28	29.1311	-31	6	46.2950	28.530	1322.551
—	—	374.000	791.000	807.628	432.045	3	28	29.3594	-31	6	18.9391	28.786	1256.398
285.500	288.800	242.300	1243.516	369.412	602.818	3	28	30.1653	-31	4	45.2669	27.441	1175.209
239.010	249.688	196.177	1204.631	412.298	645.549	3	28	30.9816	-31	4	51.3506	28.233	1300.676
178.538	583.594	135.326	1537.811	85.311	735.050	3	28	31.0125	-31	3	43.4550	27.660	1205.614
186.534	532.619	144.680	1489.280	134.119	722.071	3	28	31.0151	-31	3	53.5693	28.410	1287.140
235.011	156.803	193.406	1111.212	505.390	640.802	3	28	31.2863	-31	5	9.6016	27.989	1222.026
—	—	268.000	333.000	1273.124	497.724	3	28	32.2175	-31	7	45.5869	28.777	1185.099
114.569	494.638	71.183	1448.102	179.886	791.076	3	28	32.2364	-31	3	58.8222	27.617	991.783
—	—	192.000	702.000	912.152	605.595	3	28	32.3934	-31	6	30.1657	28.768	1244.512
—	—	162.000	700.000	916.759	635.307	3	28	32.8587	-31	6	29.5203	28.972	1382.567
—	—	90.081	725.525	897.599	709.177	3	28	33.8929	-31	6	21.9603	28.977	909.292
—	—	51.000	526.000	1099.771	730.719	3	28	35.0311	-31	6	59.9387	28.649	1169.014

<sup>a</sup>The  $x$ ,  $y$  coordinates are in pixels. N and S refer to the N and S fields as defined by the reference images. The G coordinates have their origin at the center of light of NGC 1344, and the  $x, G$  coordinate is defined along the major axis. The heliocentric radial velocities are given in  $\text{km s}^{-1}$ .